

A frequency-domain beamforming procedure for extracting Rayleigh wave attenuation coefficients and small-strain damping ratio from 2D ambient noise array measurements

Original

A frequency-domain beamforming procedure for extracting Rayleigh wave attenuation coefficients and small-strain damping ratio from 2D ambient noise array measurements / Abbas, Aser; Aimar, Mauro; Cox, Brady R; Foti, Sebastiano.
- In: EARTHQUAKE SPECTRA. - ISSN 8755-2930. - ELETTRONICO. - (2025), pp. 1-31. [10.1177/87552930241304914]

Availability:

This version is available at: 11583/2998228 since: 2025-03-11T14:46:13Z

Publisher:

Sage Publications

Published

DOI:10.1177/87552930241304914

Terms of use:

This article is made available under terms and conditions as specified in the corresponding bibliographic description in the repository

Publisher copyright

(Article begins on next page)

1 **A Frequency-Domain Beamforming Procedure for Extracting Rayleigh Wave**
2 **Attenuation Coefficients and Small-Strain Damping Ratio from 2D Ambient Noise**
3 **Array Measurements**

4 Aser Abbas,^{a, *} M.EERI, Mauro Aimar^{b)}, Brady R. Cox,^{c)} M.EERI, and Sebastiano Foti^{b)}

5 The small-strain damping ratio plays a crucial role in assessing the response of
6 soil deposits to earthquake-induced ground motions and general dynamic
7 loading. The damping ratio can theoretically be inverted for after extracting
8 frequency-dependent Rayleigh wave attenuation coefficients from wavefields
9 collected during surface wave testing. However, determining reliable estimates
10 of in-situ attenuation coefficients is much more challenging than achieving
11 robust phase velocity dispersion data, which are commonly measured using
12 both active-source and ambient-wavefield surface wave methods. This paper
13 introduces a new methodology for estimating frequency-dependent attenuation
14 coefficients through the analysis of ambient noise wavefield data recorded by
15 two-dimensional (2D) arrays of surface seismic sensors for the subsequent
16 evaluation of the small-strain damping ratio. The approach relies on the
17 application of an attenuation-specific wavefield conversion and frequency-
18 domain beamforming. Numerical simulations are employed to verify the
19 proposed approach and inform best practices for its application. Finally, the
20 practical efficacy of the proposed approach is showcased through its application
21 to field data collected at a deep, soft soil site in Logan, Utah, USA, where phase
22 velocity and attenuation coefficients are extracted from surface wave data and
23 then simultaneously inverted to develop deep shear wave velocity and damping
24 ratio profiles.

25 **Keywords:** attenuation; damping; surface wave testing; inversion; in situ; noninvasive;
26 ambient noise; vibrations

27
28
29 ^{a)} University of Rhode Island, Department of Civil and Environmental Engineering, Kingston, RI, USA, 02882

30 ^{b)} Politecnico di Torino, Department of Structural, Building and Geotechnical Engineering (DISEG), Torino,
31 Italy.

32 ^{c)} Utah State University, Department of Civil and Environmental Engineering, Logan, UT, USA, 84322.

33
34 **Corresponding author:**

35 Aser Abbas, 2 East Alumni Avenue, Kingston, RI, 02881

36 E-mail: aser.abbas@uri.edu

37 INTRODUCTION

38 The small-strain shear modulus (G_{max}) and small-strain damping ratio (D) form the starting
39 point for many soil constitutive models and play a crucial role in assessing the response of soil
40 deposits to earthquake-induced ground motions and general dynamic loading. G_{max} is directly
41 related to the in-situ shear wave velocity (V_s), and it represents the soil stiffness and its
42 resistance to deformation under applied shear stress. D characterizes the energy dissipation
43 properties of the material at small strains. The influence of D on the amplitude and frequency
44 content of seismic waves has been recognized since at least 1940 (Ricker, 1940), with
45 subsequent research establishing it as a pivotal parameter for seismic site response studies and
46 for modeling ground-borne vibrations (e.g., Anderson et al., 1996; Tao and Rathje, 2019;
47 Papadopoulos et al., 2019; Foti et al., 2021). Despite its significance, the in-situ estimation of
48 D has received far less attention when compared to measurements of V_s (Parolai, 2014). D can
49 theoretically be inverted for after extracting frequency-dependent Rayleigh wave phase
50 velocity and attenuation coefficients (α) from wavefields collected during surface wave testing
51 (Lai, 1998; Foti, 2004). However, in-situ α values are generally much more difficult to reliably
52 measure than phase velocities (Haendel et al., 2016; Parolai et al., 2022), which are commonly
53 measured using both active-source and ambient-wavefield surface wave methods.

54 This paper introduces a new noninvasive method to estimate frequency-dependent Rayleigh
55 wave α using ambient noise wavefield data collected with two-dimensional (2D) arrays of
56 surface seismic sensors for the subsequent evaluation of D . The approach relies on frequency-
57 domain beamforming (FDBF) and applies an attenuation-specific wavefield conversion,
58 known as the FDBFa approach. While Aimar et al. (2024a) previously used this approach for
59 active-source surface wave testing, it has not been applied to ambient noise surface wave
60 testing. In this paper, we introduce a new method called the noise FDBFa (NFDBFa) approach
61 and document its development and application.

62 The subsequent sections of this paper are organized as follows: first, we cover important
63 background information on attenuation and damping. Second, we present a concise overview
64 of the FDBF technique introduced by Lacoss et al. (1969) and the FDBFa wavefield conversion
65 methodology proposed by Aimar et al. (2024a), along with the integration of these methods
66 within our proposed NFDBFa approach. Then, synthetic studies are presented to showcase the
67 capabilities of the proposed NFDBFa approach and inform best practices for its application.
68 The synthetic studies offer valuable insights into the influence of 2D array size and proximity

69 to noise sources on attenuation estimates. For example, it is demonstrated that the optimal 2D
70 ambient noise array design principles for attenuation estimation differ from the principles
71 governing 2D array design for phase velocity estimation. Finally, we demonstrate the practical
72 utility of our proposed NFDBFa technique through a field application at a deep, soft soil site
73 in Logan, Utah, USA. In this field application, phase velocity and attenuation coefficients are
74 extracted from surface wave data and then simultaneously inverted to develop deep V_s and D
75 profiles. The good agreement observed between the attenuation estimates derived from our
76 new NFDBFa technique and those obtained through the standard FDBFa analysis of active-
77 source data collected using the multichannel analysis of surface waves (MASW) provides
78 compelling evidence of the effectiveness of our new ambient noise approach.

79 **BACKGROUND**

80 Seismic wave attenuation is commonly attributed to three mechanisms: material damping,
81 geometric spreading, and apparent attenuation (Zywicki, 1999). Material damping, or anelastic
82 attenuation, arises from the collective interaction of diverse mechanisms (Johnston et al.,
83 1979). These factors encompass frictional losses among solid particles and fluid flow losses
84 due to the relative motion between solid and fluid phases, a phenomenon particularly notable
85 in coarse-grained soils (Biot, 1956; Walsh, 1966 and 1968; Stoll, 1974). Fine-grained soils,
86 however, showcase more intricate phenomena influenced by electromagnetic interactions
87 between water dipoles and microscopic solid particles (Lai, 1998). This intrinsic material
88 damping is typically approximated as frequency-independent (i.e., hysteretic), particularly
89 within the frequency range spanning 0.1 to 10 Hz (Aki and Richards, 1980; Shibuya et al.,
90 1995), commonly considered in seismic site response studies. However, the assumption that
91 material damping is frequency-independent is debated in the literature, as discussed by Lai and
92 Özcebe (2016) and the references therein.

93 The attenuation of seismic waves due to material damping in a continuum is related to the
94 damping ratios of both compression waves (D_p) and shear waves (D_s). Researchers have
95 proposed widely variable assumptions about the relationship between D_s and D_p , with many
96 simply assuming D_s equal to D_p (Badsar et al., 2010; Verachtert et al., 2017; Aimar et al.,
97 2024b), some assuming D_s less than D_p (Bergamo et al., 2023), and some D_s greater than D_p
98 (Xia et al., 2002). Although theoretically, D_s can be less than, equal to, or greater than D_p
99 depending on soil types and conditions (e.g., degree of saturation) (Winkler and Nur, 1982;
100 Menq, 2003), these assumptions have typically been made somewhat arbitrarily due to a lack

101 of in-depth studies that provide guidelines on how to accurately measure or reasonably assume
102 in-situ D_s and D_p values. The damping ratio (D) is commonly used in engineering, while its
103 inverse, the quality factor (Q), where $Q^{-1} = 2D$, is more prevalent in seismological and
104 geophysical literature (Foti, 2004). Q , being the inverse of D , also differs for compressional
105 waves (Q_p) and shear waves (Q_s).

106 Geometric or radiation damping involves the spread of a fixed amount of energy over a broader
107 area or volume as the wavefront moves away from the source. Take, for instance, a harmonic
108 unit point load applied along the normal direction to the surface of a homogeneous and
109 isotropic half-space; this perturbation generates both body waves and Rayleigh waves. The
110 body waves propagate radially from the source, forming a hemispherical wave front, while
111 Rayleigh waves travel outward along a cylindrical wave front. As these waves travel, they
112 traverse an expanding volume of material, leading to a decrease in energy density as the
113 distance from the source increases. In the interior of the half-space, the amplitude of the body
114 waves attenuates in proportion to r^{-1} (where r is the radial distance from the source). However,
115 along the surface of the half-space, the amplitude of body waves attenuates proportionally to
116 r^{-2} . Conversely, the amplitude of the Rayleigh waves attenuates as $r^{-0.5}$ (Lamb, 1904; Ewing
117 et al., 1957; Richart et al., 1970). Consequently, at substantial distances from the surface source,
118 the dominant influence on overall particle motion stems from the surface wavefield (Lai, 1998).
119 It is worth mentioning that these geometric spreading rules do not hold with transient
120 waveforms (Keilis-Borok, 1989) or non-homogeneous media (Lai, 1998).

121 Apparent attenuation includes wave scattering, which arises from the interaction of waves with
122 heterogeneities along the seismic path (O'Doherty and Anstey, 1971; Spencer et al., 1977), as
123 well as the reflection and transmission of seismic waves at interfaces and mode conversions
124 (Rix et al., 2000). Therefore, apparent attenuation is highly site-specific and difficult to
125 generalize.

126 Multiple approaches have been proposed to characterize the attenuation of seismic waves. One
127 such technique involves the spectral decay parameter, kappa (κ), which describes the amplitude
128 decay of the ground motion acceleration spectrum at high frequencies. κ and its site-specific
129 and source/path components encapsulate various damping mechanisms, including material
130 damping and wave scattering (e.g., Anderson and Hough, 1984; Ktenidou et al., 2015; Parolai
131 et al., 2022). Laboratory tests and in-situ methods have also been proposed to estimate D .

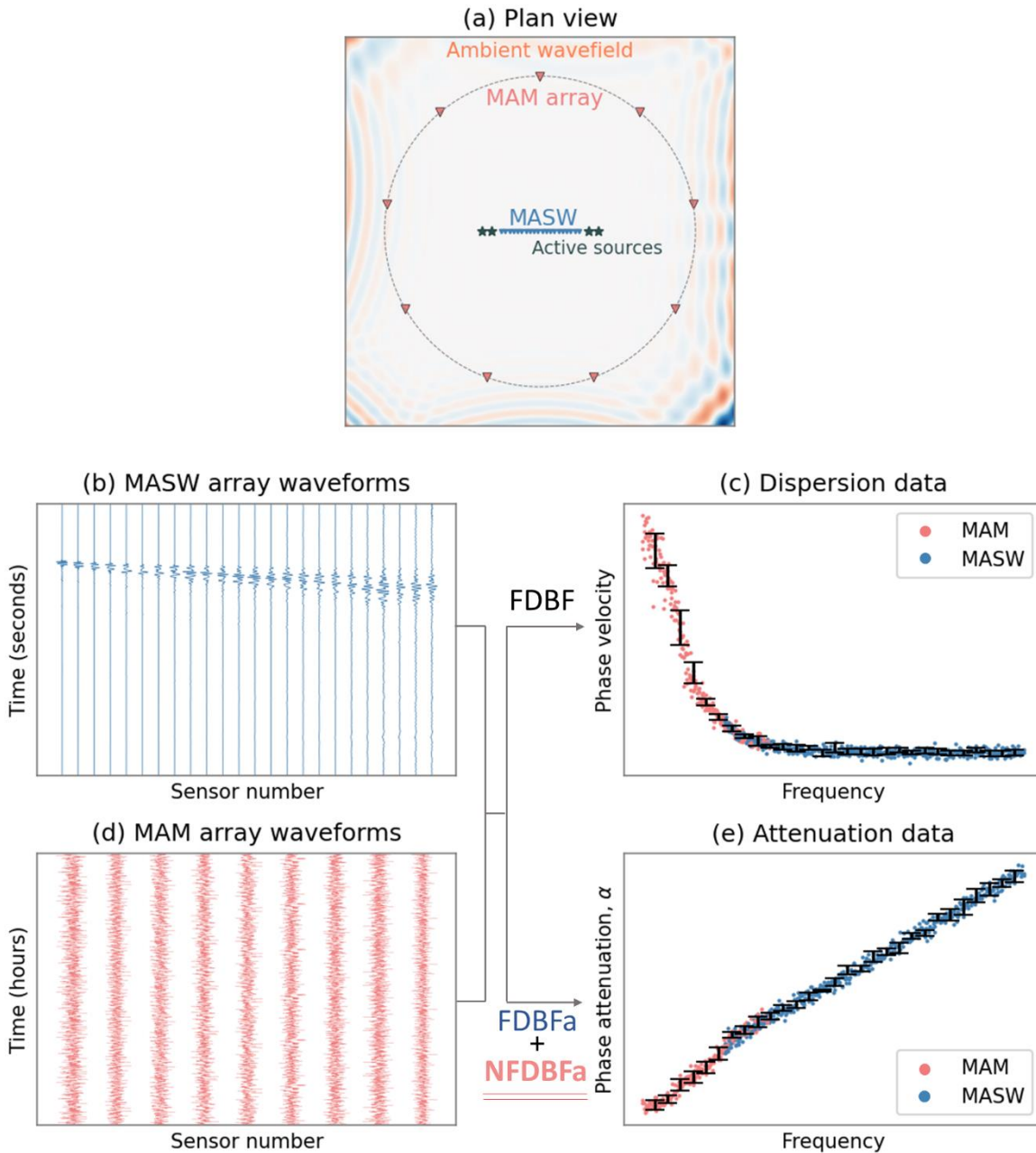
132 Laboratory tests, such as the resonant column (ASTM D4015-21), are valuable for
133 parametrically studying the material/intrinsic damping ratio, but they cannot capture the other
134 two mechanisms contributing to the attenuation of seismic waves in situ. Conversely, the
135 damping ratio estimates obtained using in-situ methods are generally influenced by all the
136 seismic wave damping mechanisms mentioned above (Parolai et al., 2022). In-situ methods
137 also have the advantage of assessing soil characteristics in their natural and undisturbed state
138 (Rix et al., 2000). Additionally, in-situ tests encompass a greater soil volume, effectively
139 reducing result biases that might arise from localized variations in soil properties (Badsar et
140 al., 2010). Furthermore, they provide parameter estimates on a spatial scale relevant to common
141 engineering applications (e.g., Comina et al. 2011). In the scope of estimating D , in-situ
142 methods can be dissected into two categories: invasive and noninvasive methods. Invasive
143 methods encompass techniques such as cross-hole testing (Jongmans, 1989; Hall and Bodare,
144 2000) and downhole testing (Michaels, 1998; Crow et al., 2011). Noninvasive methods,
145 particularly surface wave techniques, offer numerous advantages. By situating sensors at the
146 ground surface, surface wave methods accelerate data acquisition, minimize costs, streamline
147 validation of soil-receiver coupling, and encompass a frequency range closely aligned with
148 those pertinent to earthquake engineering applications (Rix et al., 2000; Verachtert et al., 2017;
149 and Parolai et al., 2022).

150 Surface wave testing became popular in the 1980's as an effective way to non-invasively
151 develop 1D layering and V_s profiles for both soil deposits and pavement systems (e.g., Nazarian
152 et al., 1983; Stokoe et al., 1989). Typically, the use of surface wave methods involves acquiring
153 experimental phase velocity dispersion data through active-source methods, ambient-noise
154 methods, or a combination of both (Tokimatsu, 1995). These dispersion data are then inverted
155 to obtain layered subsurface models, with the primary goal of resolving changes in V_s . The
156 combined use of active-source and ambient-noise methods facilitates the generation of
157 dispersion data across a wide frequency range, which enables resolution of both near-surface
158 and deeper layers. Active sources predominantly produce energy concentrated at higher
159 frequencies, typically ranging from several Hertz to perhaps 100 Hertz, with limited energy
160 generation below 5-10 Hz for small sources like sledgehammers and lightweight drop weights.
161 Consequently, the effective profiling depth using active-source methods is often constrained to
162 approximately 15 to 40 m, contingent on the subsurface velocity and source mass (Foti et al.,
163 2018). The primary hindrance to achieving increased penetration depths lies in generating

164 lower frequency (i.e., longer wavelength) waves with affordable and highly-portable sources.
165 This difficulty is circumvented by ambient-noise methods, which do not involve the active
166 generation of wave energy. Instead, they rely on ground motions induced by cultural noise and
167 microtremors (i.e., ambient noise), encompassing an abundance of low-frequency components
168 (Lai, 1998). Consequently, ambient-noise surveys offer valuable insights for deep
169 characterization, extending to depths of hundreds of meters or more (Foti et al., 2014; Teague
170 et al., 2018a). Nevertheless, the spectral power of microtremors is generally low at higher
171 frequencies (Peterson, 1993), which limits their ability to resolve changes in stiffness near the
172 ground surface (Tokimatsu, 1995; Foti et al., 2014). Combining both active and ambient-noise
173 measurements offers a solution to overcome this limitation.

174 Ambient-noise surveys typically employ 2D arrays of surface seismic sensors due to the a-
175 priori unknown location of the ambient noise sources. Unlike linear arrays, 2D arrays allow for
176 the determination of wave propagation direction, which is necessary for resolving the true
177 phase velocity (Cox and Beekman, 2011). While 2D ambient noise array measurements have
178 been referred to using several names, in this paper we will refer to them as microtremor array
179 measurements (MAM; Ohrnberger et al., 2004; Teague et al., 2018b). A schematic
180 representation of a typical survey utilizing both active and ambient-noise arrays is presented in
181 Figure 1a. The active-source array in Figure 1a is in accordance with the MASW method (Park
182 et al., 1999), utilizing a linear array of receivers to capture the wavefield generated by active
183 sources off each end of the array. Example waveforms recorded by 24 receivers placed in-line
184 with one of the active sources to the left of the array are depicted in Figure 1b. The ambient
185 wavefield array depicted in Figure 1a is in accordance with MAM testing, where surface
186 sensors are deployed in a 2D circular pattern (note that other 2D geometries are also
187 permissible). Example ambient noise waveforms recorded by nine sensors in the circular array
188 are depicted in Figure 1d. Figure 1c schematically illustrates phase velocity dispersion data
189 that are commonly extracted from active-source MASW waveforms and ambient noise MAM
190 waveforms using various well-known wavefield transformation techniques (Vantassel and
191 Cox, 2022). Examples of these techniques include frequency-domain beamforming (FDBF;
192 Lacoss et al., 1969), high-resolution frequency-wavenumber (f-k) spectrum analysis (Capon
193 1969), cylindrical FDBF (Zywicki 1999; Zywicki and Rix, 2005), and Rayleigh three-
194 component beamforming (Wathelet et al., 2018). The combined dispersion data from MASW
195 and MAM spans a wide frequency range, encompassing both low frequencies obtained from

196 the MAM testing and high frequencies obtained from the MASW testing, with some overlap
 197 in between. The phase velocity dispersion data are then typically used to solve the parameter
 198 identification problem (i.e., inversion) and obtain 1D V_s profiles of the subsurface (Foti et al.,
 199 2018; Vantassel and Cox, 2021). Note that the inversion step and resulting V_s profiles are not
 200 illustrated schematically in Figure 1.



201

202 **Figure 1.** Schematic illustrating the data acquisition and processing stages of active-source and
 203 ambient-wavefield surface wave testing used to extract phase velocity and phase attenuation data. Panel
 204 (a) presents a typical acquisition setup consisting of concentric MASW and MAM arrays, featuring
 205 active sources for the MASW array and an ambient wavefield for the MAM array. Panel (b) shows

206 waveforms from a single active-source location collected using the MASW array, while Panel (c)
207 presents the combined phase velocity dispersion data resulting from MASW and MAM Frequency
208 Domain Beamforming (FDBF) processing. Panel (d) depicts the ambient noise waveforms collected
209 from the MAM array. In Panel (e), phase attenuation data processed through active-source FDBFa and
210 ambient-wavefield NFDBFa techniques are illustrated.

211 As noted above, much more effort has been devoted to extracting phase velocity information
212 from surface wave approaches than to extracting attenuation information. Nonetheless,
213 multiple active-source methods have been developed to estimate the attenuation of surface
214 waves. The methods introduced by Lai (1998), Lai et al. (2002), Rix et al. (2000), Xia et al.
215 (2002), and Foti (2004) are founded on assessing the spatial decay of Rayleigh waves, a
216 phenomenon that is influenced by both D_p and D_s , as described by Aki and Richards (1980).
217 These approaches assume the dominance of a single Rayleigh wave mode of propagation.
218 Consequently, they might yield inaccurate results in soil profiles where multiple surface wave
219 modes significantly contribute to the wavefield propagation (Rix et al. 2001). Badsar et al.
220 (2010) introduced the half-power bandwidth method, originally developed in the field of
221 mechanical and structural dynamics to determine the modal damping ratio of a structure, to
222 assess Rayleigh modal attenuation by analyzing the width of the Rayleigh peaks in the f-k
223 domain. Verachtert et al. (2017) employed the circle fit method, originally developed to
224 determine eigenfrequencies and modal damping ratios in structural dynamics (Ewins 1984), to
225 estimate multimodal Rayleigh dispersion and attenuation curves. Both the half-power
226 bandwidth and circle fit methods facilitated the determination of modal attenuation curves from
227 multimode wavefields (Verachtert et al., 2017). Recently, Aimar et al. (2024a) introduced an
228 innovative technique that combines a novel wavefield conversion approach coupled with
229 FDBF (Lacoss et al., 1969) for processing active-source data collected using MASW to
230 estimate the frequency-dependent α values. They called this the FDBF attenuation (FDBFa)
231 method. Notably, the wavefield conversion proposed by Aimar et al. (2024a) to extract α differs
232 from the conventional wavefield transformations commonly used to go from the time-distance
233 domain to the f-k domain, as detailed in the following section. To avoid confusion, we will
234 refer to the wavefield transformation proposed by Aimar et al. (2024a) as ‘wavefield
235 conversion,’ while reserving the term ‘wavefield transformation’ specifically for the more
236 common f-k domain transformations used to extract phase velocity data.

237 While important research on extracting phase attenuation coefficients using active-source
238 methods is ongoing, similar to phase velocity data, combining active-source and ambient noise
239 methods is desirable for resolving attenuation data over a broader frequency band. The majority

240 of ambient noise techniques aimed at estimating the attenuation of surface waves were
241 developed for regional-scale estimation (Haendel et al., 2016; Parolai et al., 2022). Only a
242 limited number of approaches have considered local scales that hold relevance for engineering
243 purposes, like site-specific seismic ground response analyses or dynamic vibration studies.
244 These local-scale approaches are predominantly based on retrieving attenuation properties
245 from the cross-correlation of seismic noise (e.g., Albarello and Baliva, 2009; Parolai, 2014;
246 Haendel et al., 2016). Albarello and Baliva (2009) proposed a methodology that reconstructs
247 the Green's function based on the temporal derivative of averaged cross-correlations from
248 noise recordings obtained by pairs of geophones, thereby incorporating attenuation effects into
249 the process. They further validated this approach by demonstrating its potential in estimating
250 attenuation coefficients at two distinct sites. Parolai (2014) estimated the Rayleigh phase
251 velocity and attenuation coefficients by fitting a damped zero-order Bessel function, introduced
252 by Prieto et al. (2009), using data generated from the space correlation function introduced by
253 Aki (1957). To mitigate the impact of uneven source distribution on cross-correlations, Haendel
254 et al. (2016) employed a higher-order noise cross-correlation technique to extract the phase
255 velocity and attenuation coefficient of Love waves. They illustrated that their approach yields
256 correlation functions with higher signal-to-noise ratios compared to simple noise cross-
257 correlations.

258 The importance of seismic noise cross-correlation methods cannot be underestimated.
259 Nonetheless, in theory, the reconstruction of the full Green's function requires the noise
260 wavefield energy to be equally partitioned in all directions (Sánchez-Sesma and Campillo,
261 2006; Snieder et al., 2007). This is a highly specific condition that is rarely met rigorously by
262 ambient noise on Earth (Cupillard and Capdeville, 2010; Tsai, 2011; Haendel et al., 2016).
263 Furthermore, while travel time measurements from cross-correlation of ambient noise are
264 theoretically understood, amplitude measurements lack a corresponding theoretical
265 background, except when the noise is equipartitioned (Snieder et al., 2007; Tsai, 2011). Studies
266 by Cupillard and Capdeville (2010) and Tsai (2011) have shown that attenuation estimates
267 using cross-correlations are significantly influenced by the distribution of the noise sources. In
268 light of the challenges posed by the equipartitioning condition for the reconstruction of the full
269 Green's function in ambient noise studies (Sánchez-Sesma and Campillo, 2006; Snieder et al.,
270 2007), and considering the limitations highlighted by Cupillard and Capdeville (2010) and Tsai
271 (2011) regarding the influence of noise source distribution on attenuation estimates, we

272 introduce a paradigm-shifting approach herein for calculating attenuation coefficients from
273 ambient noise. This novel method not only eliminates the need for an equipartitioned noise
274 wavefield, but also remains robust in the face of uneven noise source distribution, marking a
275 departure from existing methodologies.

276 This paper builds upon Aimar et al.'s (2024a) work on developing an FDBFa technique for
277 estimating α from active-source MASW testing and expands the FDBFa approach to ambient
278 noise data recorded using MAM. Importantly, using an FDBF approach enables the actual
279 direction of ambient noise propagation to be determined for each noise window and frequency,
280 and does not require equipartitioning of ambient noise energy. Furthermore, using an FDBF
281 approach enables the phase attenuation data generated from MASW and that from MAM to be
282 combined in order to generate phase attenuation data spanning a broader frequency range, as
283 illustrated schematically in Figure 1e. The experimental dispersion and attenuation data can
284 then be combined and inverted to determine not only the V_s profile but also the D profile of the
285 subsurface to greater depths. This inversion of dispersion and attenuation data to obtain V_s and
286 D profiles can be carried out either sequentially, as demonstrated in the work of Rix et al.
287 (2000), or simultaneously, as shown by both Lai (1998) and Aimar et al. (2024b).

288 **WAVEFIELD CONVERSION PROPOSED BY AIMAR ET AL., (2024A)**

289 The method introduced by Aimar et al. (2024a) to estimate Rayleigh wave attenuation (α)
290 assumes that the recorded wavefield is dominated by planar surface waves, specifically
291 Rayleigh waves observed in the far field, with a dominant propagation mode. Several
292 techniques have been developed to estimate the wavenumber (k) and therefore the phase
293 velocity from such wavefields (e.g., Lacoss et al., 1969; Capon, 1969; Zywicki and Rix, 2005;
294 Wathelet et al., 2018). Aimar et al. (2024a) harnessed this concept and introduced a novel
295 wavefield conversion approach that provides a pathway for calculating α by utilizing methods
296 from existing literature originally developed for estimating k . The methodology involves
297 converting the recorded wavefield into a function interpreted as a pseudo-wave. This pseudo-
298 wave exhibits dispersion characteristics reflecting the phase attenuation of the original wave.
299 The determination of α then becomes straightforward through the application of existing
300 techniques for estimating k .

301 Consider the harmonic, exponentially decaying displacement wavefield, $U(r)$, depicted in
302 Figure 2a and expressed by Equation 1. This wavefield is observed at several discrete distances

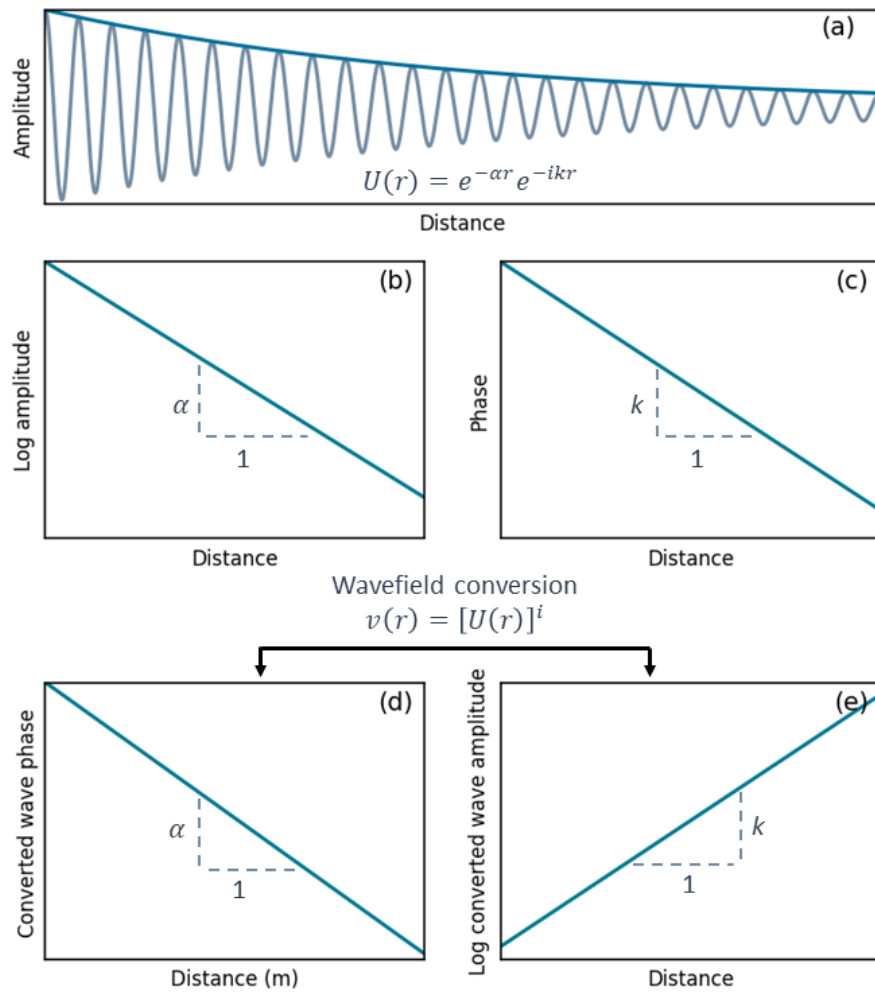
303 at a specific moment in time and is induced by the passage of a monochromatic plane wave.
304 Within this wavefield, α governs the amplitude decay resulting from material damping in
305 accordance with a viscoelastic constitutive model with no geometric spreading. When the
306 wavefield is plotted as log amplitude versus radial distance (r) from the source, the slope of
307 the amplitude decay is α , as illustrated in Figure 2b. When the wavefield is plotted as phase
308 angle versus r , k denotes the slope of the unwrapped phase (i.e., the linear phase shift), as
309 shown in Figure 2c. Aimar et al. (2024a) proposed raising the recorded wavefield, $U(r)$, to the
310 power of the imaginary number, i (see Equation 2). Consequently, a pseudo displacement
311 wavefield, $v(r)$, is generated, wherein the wavenumber is modulated by α , signifying that
312 when the unwrapped phase of the converted wavefield is graphed against radial distance, the
313 slope of that phase corresponds to the value of α (refer to Figure 2d). Conversely, when the log
314 amplitude of the converted wavefield is plotted against distance, the slope manifests as k , with
315 an inverted sign (refer to Figure 2e). This wavefield conversion allows for estimating α using
316 any of the already established and common wavefield transformation techniques for calculating
317 k (e.g., f-k or FDBF methods).

$$318 \quad U(r) = e^{-\alpha r} e^{-ikr} \quad (1)$$

319

$$320 \quad v(r) = [U(r)]^i = e^{-i\alpha r} e^{kr} \quad (2)$$

321 This wavefield conversion can also be extended to a broadband wavefield, comprised of a
322 superposition of monochromatic plane waves by exponentiating the wavefield in the frequency
323 domain with the power of the imaginary number. To address numerical artifacts introduced by
324 the wrapped phase on the pseudo wavefield, Aimar et al. (2024a) recommended normalizing
325 $v(r)$ by its amplitude on a frequency-by-frequency basis. Aimar et al. (2024a) showed that this
326 wavefield conversion can be successfully applied to active-source wavefields recorded using
327 MASW as a means to estimate α . In this paper, we extend this approach to estimate α from
328 ambient noise wavefields recorded using MAM arrays, employing the FDBF technique
329 introduced by Lacoss et al. (1969).



330

331 **Figure 2.** Schematic illustrating the wavefield conversion approach proposed by Aimar et al. (2024a)
 332 to extract attenuation coefficients (α). Panel (a) displays the particle displacement of a monochromatic
 333 plane wave experiencing exponential amplitude decay with distance, indicative of material damping in
 334 a viscoelastic constitutive model. Panel (b) depicts linear amplitude decay in log amplitude versus linear
 335 distance space, where the slope represents the phase attenuation coefficient. In Panel (c), the slope of
 336 the unwrapped phase, corresponding to the wavenumber (k), is shown. Panel (d) illustrates that the
 337 unwrapped phase slope is equal to the phase attenuation coefficient in the converted wavefield. Panel
 338 (e) showcases the control of the slope of the log amplitude decay with linear distance by the
 339 wavenumber, albeit with an inverted sign.

340

341 NOISE FREQUENCY DOMAIN BEAM FORMING - ATTENUATION (NFDBFa)

342 The inherent challenge in ambient noise measurements stems from the lack of *a priori*
 343 information about the source location or the direction of wave propagation, necessitating the
 344 use of spatial 2D arrays to determine the noise propagation directions during post-processing
 345 (Zywicki, 1999). As ambient noise wavefields operate in two spatial dimensions (e.g., x and
 346 y), it is necessary to represent the wavenumber using 2D vectors (Johnson and Dudgeon, 1993;

347 Zywicki, 1999), like $\mathbf{k} = k_x \hat{i} + k_y \hat{j}$, and \hat{i} and \hat{j} are unit vectors in the x and y directions,
348 respectively. Similarly, $\vec{\alpha}$ is also expressed as a 2D vector (i.e., $\boldsymbol{\alpha} = \alpha_x \hat{i} + \alpha_y \hat{j}$) in this paper.
349 Beamforming refers to a diverse set of array processing algorithms that concentrate the signal-
350 capturing capabilities of the array in a specific direction. The fundamental concept behind
351 beamforming is straightforward: when a propagating signal exists within an array's aperture,
352 the outputs of the sensors, delayed by appropriate amounts and added together, enhance the
353 coherent signal while mitigating the incoherent signal from waves propagating in different
354 directions. The delays that enhance the signal are directly linked to the time it takes for the
355 signal to travel between sensors (Johnson and Dudgeon, 1993). Delays in the time domain
356 correspond to linear phase shifts in the frequency domain, providing information about the
357 wavenumber. FDBF calculations are exclusively performed within the frequency domain.
358 Applying FDBF to the original wavefield, $U(\mathbf{r})$, provides information about \mathbf{k} , which informs
359 the estimation of the phase velocity. This paper aims to demonstrate that applying FDBF to the
360 converted, normalized pseudo wavefield, $v(\mathbf{r})$, informs the estimation of $\boldsymbol{\alpha}$. Henceforth, in this
361 paper, we will denote FDBF applied to the converted noise wavefield as NFDBFa, emphasizing
362 its role in estimating the phase attenuation from ambient noise.

363 In the NFDBFa approach, the first step is to partition the noise data collected by a 2D array of
364 m sensors into B time windows. The m sensors are located at the ground surface at coordinates
365 (x_i, y_i) denoted by the vector \mathbf{r}_i , where i varies from 1 to m . For each time window, Fourier
366 spectra are calculated. Following this, the complex number at each frequency in the spectra is
367 exponentiated to the imaginary power. Then, each exponentiated complex number is
368 normalized by dividing it by its absolute amplitude. This process is conducted to obtain the
369 normalized spectra of the pseudo wavefield (Aimar et al., 2024a). These spectra are then used
370 to compute the Hermitian symmetric spatio-spectral correlation matrix, R_{ij} , with i and j
371 representing indices of the m sensors in the 2D array, using Equation 3:

$$372 \quad R_{ij}(\omega) = \frac{1}{B} \sum_{n=1}^B v_{i,n}(\omega) v_{j,n}^*(\omega) \quad (3)$$

373 where $R_{ij}(\omega)$ is the averaged pseudo cross-power spectrum between the i^{th} and j^{th} sensors in
374 the array across all windows, $v_{i,n}(\omega)$ is the normalized pseudo spectra of the i^{th} sensor's data
375 in the n^{th} window, $*$ indicates complex conjugation, and ω is the angular frequency. Despite
376 being frequency-dependent, the spatio-spectral correlation matrix conveys spatial wavefield
377 properties. Power within specific frequency-phase attenuation (f - $\boldsymbol{\alpha}$) pairs is determined by

378 steering the array towards various directions and phase attenuation values. Array steering
 379 involves exponential phase shift vectors determined by trial α values in pseudo space, as given
 380 by Equation 4:

$$381 \quad e(\alpha) = [\exp(-i\alpha \cdot \mathbf{r}_1), \dots, \exp(-i\alpha \cdot \mathbf{r}_m)]^T \quad (4)$$

382 where $e(\alpha)$ is a steering vector associated with a trial α and T denotes the transpose of the
 383 vector. The power in a particular f - α pair, $P_{NFDBFa}(\alpha, \omega)$, is estimated by multiplying $R_{ij}(\omega)$
 384 by $e(\alpha)$ and summing the total power over all sensors, as given by Equation 5:

$$385 \quad P_{NFDBFa}(\alpha, \omega) = e^H(\alpha)R_{ij}(\omega)e(\alpha) \quad (5)$$

386 where H indicates the Hermitian transpose. The steering vectors aim to align the array with
 387 plane waves propagating from a specified direction and phase attenuation for each frequency.
 388 The successful alignment results in a peak within the $P_{NFDBFa}(\alpha, \omega)$ pseudo-spectrum
 389 estimate. Thus, the NFDBFa technique presented herein allows for estimating α from ambient
 390 noise data without requiring an equipartitioned wavefield.

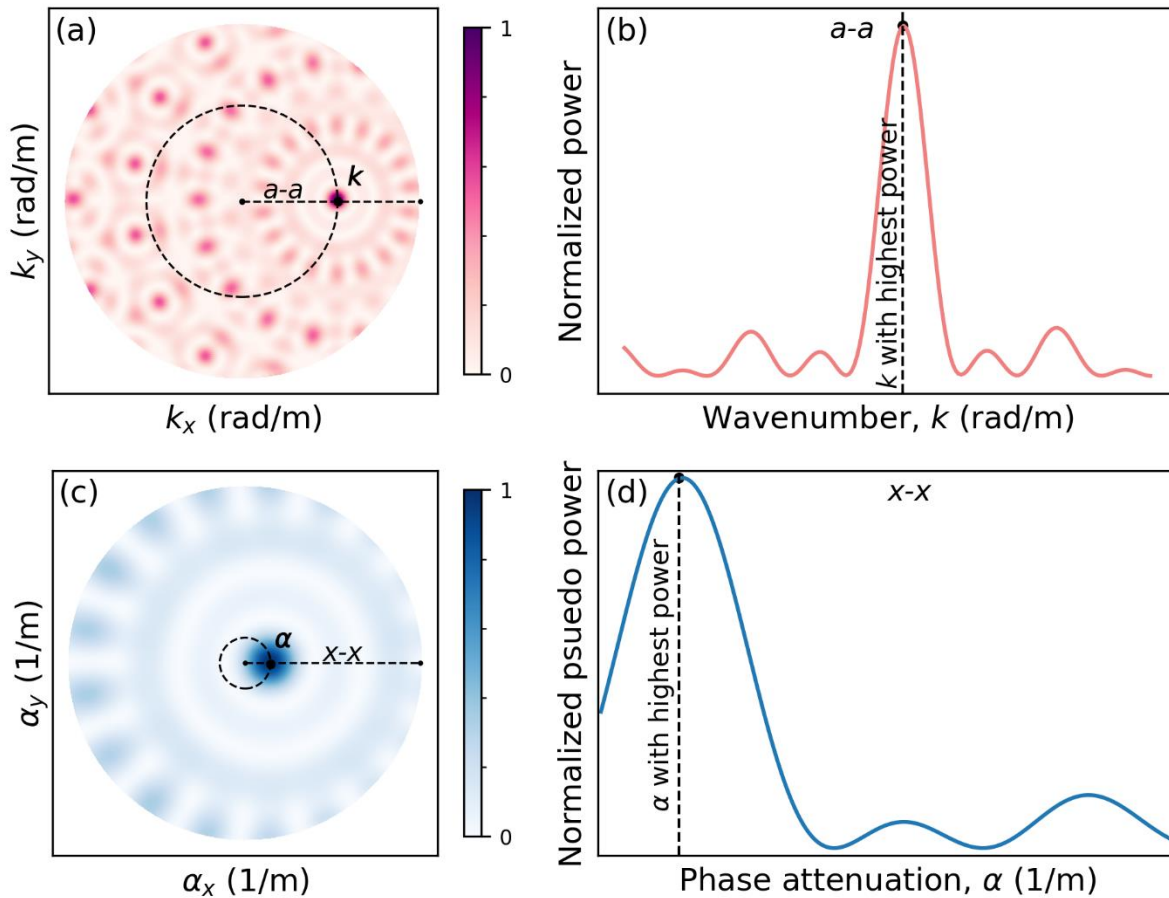
391 Even though there are similarities between the FDFBa method proposed by Aimar et al.
 392 (2024a) for estimating α using an MASW test setup and the NFDBFa method introduced in
 393 this study, there are notable differences between the two. Part of the difference is a consequence
 394 of the inherent dissimilarities between MASW and MAM. In the FDFBa method, the source
 395 location is predetermined and the array is aligned with the source, simplifying the problem and
 396 enabling the use of wavefield transformations like cylindrical frequency domain beamforming
 397 (Zywicki and Rix, 2005). Moreover, the signal-to-noise ratio can be readily enhanced by time-
 398 domain or frequency-domain stacking, as advocated by Foti et al., (2018) and Vantassel and
 399 Cox (2022). Additionally, dispersion and attenuation uncertainties can be quantified using the
 400 multiple source offset approach proposed by Cox and Wood (2011). In contrast, the NFDBFa
 401 approach developed in this study encounters distinct challenges, primarily arising from the *a*
 402 *priori* unknown location of the source(s). This necessitates the utilization of 2D arrays and
 403 involves azimuthally scanning the 2D space to ascertain the direction of the most coherent
 404 source of energy at each frequency for each window. Furthermore, the enhancement of the
 405 coherent noise-to-incoherent noise ratio involves averaging multiple time windows, while
 406 uncertainty quantification involves analyzing various time blocks, each composed of different
 407 windows. Thus, in the NFDBFa approach, data are recorded for significantly longer durations

408 (i.e., hours) compared to FDBFa (i.e., seconds). Additionally, the NFDBFa approach relies on
409 measurements of ambient noise, which is typically assumed to be generated by sources located
410 in the far field. This implies that the ambient noise sources are far enough from the MAM array
411 for body waves to have significantly attenuated relative to surface waves, and that the surface
412 waves exhibit a plane wavefront rather than a cylindrical wavefront, which is typical near a
413 seismic energy source. If the assumption of far-field sources holds true, it helps to mitigate the
414 impact of geometric spreading, which plays a significant role on attenuation estimates near an
415 active source (Badsar, 2012). Nearfield noise sources lead to complications in extracting
416 accurate attenuation estimates, as discussed in greater detail below.

417 Figure 3 presents examples of the FDBF and NFDBFa responses obtained from a synthetic
418 wavefield recorded by a ten-receiver circular MAM array for a single frequency and single
419 time window. The array comprises nine sensors equally spaced on the perimeter of the circle
420 and one sensor in the middle. The FDBF method is utilized to estimate \mathbf{k} and the NFDBFa
421 method is utilized to estimate α . In Figures 3a and 3b, the results of applying the FDBF
422 technique to the original noise wavefield recorded by the array are depicted. Figure 3a
423 illustrates the f - \mathbf{k} spectrum at the considered frequency in a 2D wave number space (k_x - k_y).
424 Stronger powers are represented by a darker purple color. This spectrum offers insights into
425 the power and vector velocities of propagating waves. In this example, a wave propagates along
426 the x-axis with a velocity represented by a vector wave number \mathbf{k} at the chosen frequency.
427 Consequently, a spectrum peak emerges on the positive k_x axis at a distance of $|\mathbf{k}|$ from the
428 origin. The associated phase velocity can be calculated as $V_r = 2\pi f / |\mathbf{k}|$, and the wavelength,
429 λ , can be determined as $\lambda = 2\pi / |\mathbf{k}|$. Figure 3b illustrates the cross-section a-a from Figure 3a,
430 revealing the main and side lobes. Generally, the narrower the main lobe and the shorter the
431 side lobes the better the array and processing algorithm are at accurately identifying the correct
432 \mathbf{k} values for a given frequency.

433 Figures 3c and 3d display the f - α spectrum obtained from applying the NFDBFa method to the
434 converted noise wavefield for the same time window used to develop Figure 3a. In this case,
435 instead of presenting the beamforming peak powers in the k_x - k_y space, as seen in Figure 3a,
436 they are now depicted in the α_x - α_y space. This transition occurs because the phase in the
437 pseudo wavefield is modulated by α (refer to Figure 2), rather than k . Figure 3c employs a
438 different color scheme, where stronger powers are represented by darker blue colors. The f - α

439 spectrum shown in Figure 3c illustrates wave propagation for a single frequency along the x-
 440 axis with a phase attenuation represented by the vector α . Figure 3d illustrates the cross-section
 441 x-x from Figure 3c, revealing the main and side lobes along the positive x-axis (i.e., direction
 442 of wave propagation). Similar to estimating \mathbf{k} , the narrower the main lobe and the shorter the
 443 side lobes the better the array and processing algorithm are at accurately identifying the correct
 444 α values for a given frequency. The ability of the NFDBFa approach to develop phase
 445 attenuation estimates from ambient-noise recorded using MAM arrays is investigated in the
 446 following section using synthetic data.



447

448 **Figure 3.** Schematic illustrating the FDBF and NFDBFa responses obtained from an ambient noise
 449 wavefield recorded by a ten-receiver circular MAM array for a single frequency and single time
 450 window. Panel (a) presents the f - \mathbf{k} spectrum resulting from applying the FDBF method to the original
 451 wavefield, displaying the beamforming peak powers in k_x - k_y space. Panel (b) shows the cross-section
 452 a-a from Figure 3a, revealing the main and side lobes. Panel (c) presents the f - α spectrum resulting
 453 from applying the NFDBFa technique to the pseudo wavefield, presenting the beamforming peak
 454 powers in α_x - α_y space. Panel (d) illustrates the cross-section x-x from Figure 3c, showing the main and
 455 side lobes along the direction of wave propagation.

456

457 **NFDBFa EVALUATION WITH SYNTHETIC WAVEFIELDS**

458 This section uses synthetic data to validate the effectiveness of the NFDBFa approach in
459 estimating phase attenuation from ambient noise recorded using MAM arrays. Specifically, the
460 approach is tested on two soil models: a half-space model and a single layer above a half-space
461 model. All numerical simulations discussed in this section were executed using Salvus
462 (Afanasiev et al., 2019), a comprehensive 2D and 3D full-waveform modeling software suite
463 based on the spectral element method. The simulations were performed on the Texas Advanced
464 Computing Center's (TACCs) high-performance cluster Lonestar6 using two compute nodes.

465 **Half-space model**

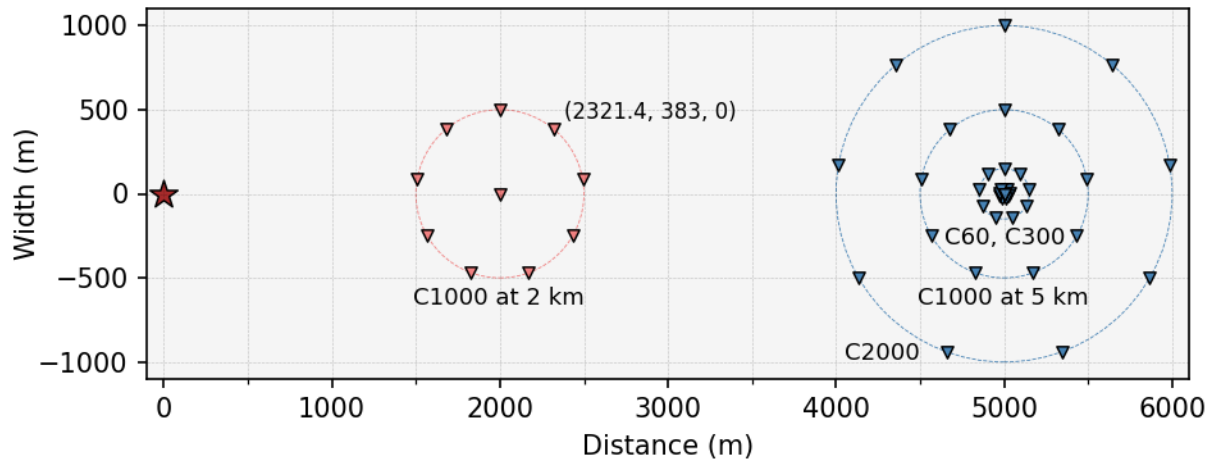
466 This subsection presents a simple wave propagation simulation consisting of a single surface
467 source generating body and surface waves propagating through a half-space soil model.
468 Despite the simplicity of the model, the outcomes obtained from this simulation offer key
469 insights into the attenuation of a wavefield generated by a surface source and elucidate the
470 capabilities of the NFDBFa approach. Figure 4 depicts a schematic plan view illustrating the
471 source location and MAM array configurations employed in the half-space simulation. The
472 wavefield was generated by a point source acting in the vertical direction at coordinates (0, 0,
473 0) in an x, y, z cartesian coordinate system. The source was a single Ricker wavelet with a
474 center frequency of 5 Hz. This source function produces broadband energy over a frequency
475 range of approximately 1 to 10 Hz. The wavefield emanating from the source was recorded
476 using five circular MAM arrays, each comprising 10 sensors, with one sensor at the center and
477 nine sensors evenly spaced around the perimeter. In this paper, the arrays are named using the
478 convention 'C' followed by the diameter of the array, where 'C' denotes that the array is circular.
479 Therefore, the first array, located two kilometers away from the source and with a diameter of
480 one kilometer, is denoted as C1000 at 2 km. The remaining four arrays, concentrically-centered
481 five kilometers from the source, have diameters of 60 m (C60), 300 m (C300), 1000 m (C1000
482 at 5 km), and 2000 m (C2000). It is noteworthy that, although currently only the vertical
483 component of the displacement wavefield is utilized in NFDBFa, each sensor recorded both
484 horizontal and vertical displacement components, and plans for utilizing all components from
485 noise recordings are ongoing. Additionally, the NFDBFa processing operated independently of
486 any knowledge about the source location, mirroring the conditions of an ambient noise MAM
487 survey, ensuring an unbiased analysis.

488 The half-space constitutive soil parameters are presented in Figure 5a, where V_p , and ν are the
489 compression wave velocity, and Poisson's ratio, respectively. The V_s , V_p , D_s , and D_p values
490 adopted in the simulations presented in this paper are within the range of values typically
491 measured in the laboratory for near surface geomaterials, such as sands, clays, and gravels
492 (Darendeli 2001; Menq 2003; Parolai et al. 2022). It is worth noting that while these specific
493 values are within reasonable limits, their overall influence on the conclusions drawn from our
494 study is limited. Due to the large spatial extent of the model and the substantial computational
495 expense associated with running a simulation over such a vast domain, a 2D simulation was
496 conducted rather than a 3D simulation. In the 2D simulations, the sensor locations were
497 projected onto a 2D plane, as illustrated in Figure 5a. This entailed setting the y-coordinate to
498 zero for each surface sensor location shown in Figure 4, resulting in their positions being
499 determined exclusively by their x-axis coordinates. For example, the sensor initially situated
500 at coordinates (2321.4, 383, 0) in an x, y, z system (as depicted in Figure 4), transformed to
501 (2321.4, 0) in the 2D x, z system presented in Figure 5. However, it is important to note that,
502 during NFDBFa processing, the coordinates assigned to each sensor were derived from those
503 shown in Figure 4; consequently, the aforementioned sensor retained coordinates of (2321.4,
504 383, 0) during processing. This approach not only substantially reduced the computational cost
505 of the simulations, but also ensured that the arrays were measuring plane waves. The simulation
506 required 4 hours and 20 minutes of computation utilizing 256 threads on the high-performance
507 cluster Lonestar6.

508 Before describing the application of the NFDBFa method, some preliminary features of the
509 amplitude decay versus distance are discussed, as they directly influence attenuation estimates.
510 To better observe this decay pattern, the wavefield emanating from the source was recorded
511 every ten meters along the free surface. Those time histories were then filtered at discrete
512 frequencies so the amplitude decay at each frequency could be observed. The decay of Fourier
513 amplitudes with distance from the vertical Ricker wavelet source for frequencies 1, 2, 3, 4, and
514 5 Hz are shown in Figures 5b and 5c. In Figure 5b, the amplitudes for each frequency are
515 normalized by their respective maximum values at the source and plotted on a log scale, while
516 the distances are not normalized and plotted on a linear scale. In contrast, in Figure 5c, the
517 distances from the source are normalized by the Rayleigh wave fundamental mode wavelength
518 (λ_R) corresponding to each plane wave frequency and plotted on a linear scale. The figures
519 depict a sharp amplitude decrease near the source due to nearfield effects. Following this,

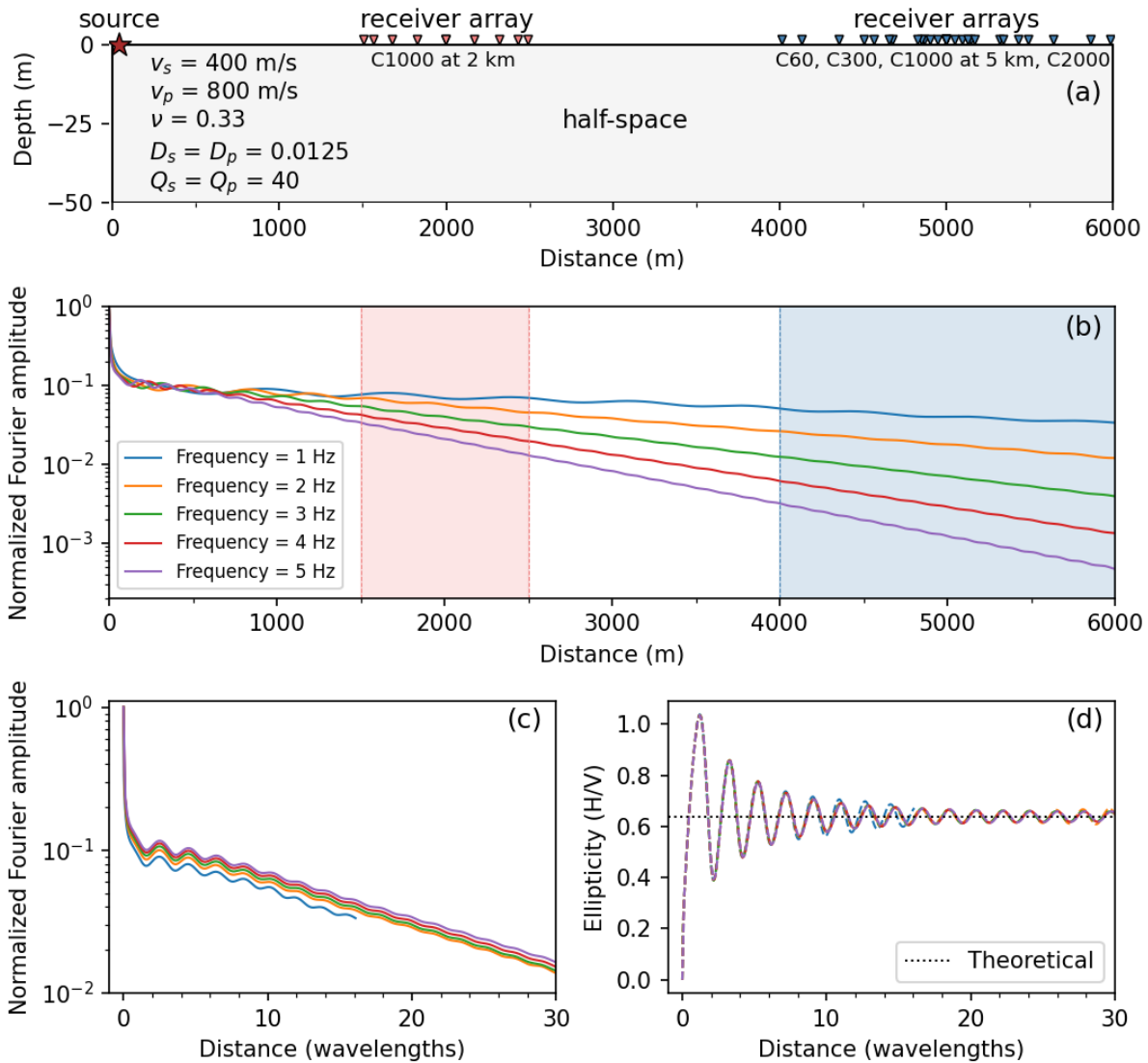
520 amplitude oscillations with diminishing power are superimposed over a linear decay trend.
521 Note that a linear decay trend in log amplitude scale corresponds to an exponential decay in
522 linear amplitude scale. These amplitude oscillations tend to flatten greatly after propagating
523 approximately $10 \lambda_R$ away from the source. It is noteworthy that these oscillations in a half-
524 space model, although verified through both 2D and 3D simulations using other software
525 packages like the ElastoDynamics Toolbox (EDT; Schevenels et al., 2009), and similarly
526 reported by Tokimatsu (1995), challenge the conventional intuition of wave attenuation in a
527 half-space. Neither the geometric spreading of Rayleigh waves nor the attenuation due to
528 material damping should exhibit such oscillations in a half-space, as detailed by Lai (1998) for
529 3D conditions. The oscillating amplitude decay pattern in a half-space model is a result of body
530 wave amplitude decay oscillations, as shown by Holzlochner (1980) and Tokimatsu (1995).
531 Hence, when estimating phase attenuation using ambient noise, it is essential for the MAM
532 arrays to be at a sufficient distance (more than approximately $10 \lambda_R$) away from any potential
533 surface sources, such that wave amplitude oscillations do not contaminate the expected trend
534 of amplitude decay with distance.

535 It is worth noting that in 3D layered media, oscillating amplitude decay of Rayleigh waves due
536 to geometric spreading has been reported and accounted for in attenuation studies, as observed
537 in the work of Lai (1998). Thus, in layered media, wave amplitude oscillations can be more
538 pronounced and may extend beyond $10 \lambda_R$ from the surface source, as demonstrated by
539 Tokimatsu (1995). This may be thought of as a type of near-field effect specific to attenuation
540 studies, wherein the wavefield amplitude decay patterns are significantly more complicated at
541 distances less than approximately $10 \lambda_R$ from source. This is distinct from, and more severe
542 than, the typical range of near-field effects for phase velocity estimations, which generally
543 deteriorate between $0.5 \lambda_R$ and $2 \lambda_R$ from the source, depending on the subsurface velocity
544 structure (Tokimatsu 1995; Rix et al., 2001).



545

546 **Figure 4.** Plan view of the source (star symbol) and receiver (inverted triangle symbols) configurations
 547 used for synthetic wavefield simulations. The source was a single Ricker wavelet with a center
 548 frequency of 5 Hz. The wavefield was recorded using five MAM arrays. The first array (C1000 at 2
 549 km) has a diameter of 1 km and is positioned 2 km from the source. The remaining four arrays are
 550 concentrically-centered 5 km away from the source and have diameters of 60 m (C60), 300 m (C300),
 551 1 km (C1000 at 5 km), and 2 km (C2000), respectively.



552

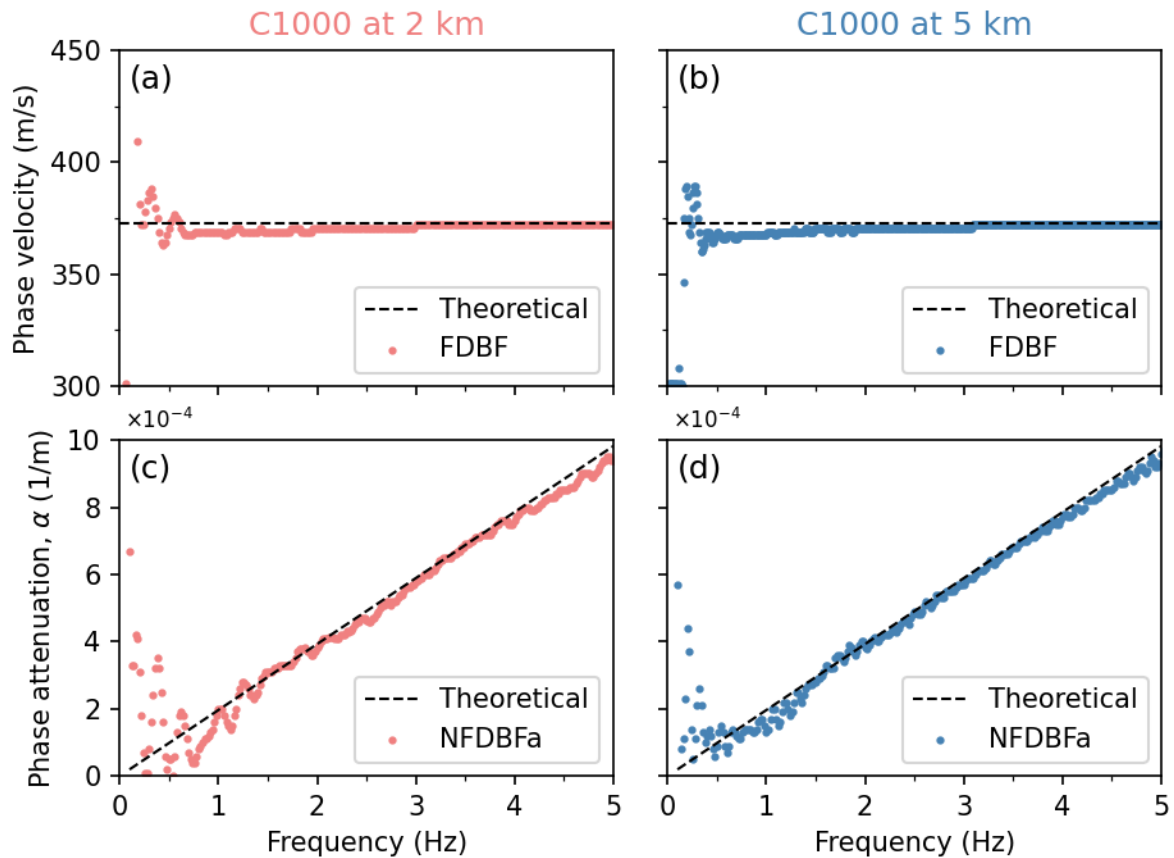
553 **Figure 5.** Homogeneous half-space wavefield simulation: Panel (a) presents a cross-section view of the
 554 configuration of the source and receivers shown in Figure 4, along with the half-space soil
 555 properties. Panel (b) shows the decay of particle vertical displacement as a function of distance from
 556 the source for five distinct frequencies, each normalized by its maximum amplitude at the source. Panel
 557 (c) presents the particle displacement decay patterns from Panel b, with distance now normalized by
 558 the wavelength for each frequency. Panel (d) shows the particle ellipticities for each frequency,
 559 expressed as the horizontal particle displacement divided by the vertical particle displacement, with the
 560 dotted horizontal line indicating the theoretical ellipticity calculated based on the Poisson's ratio of the
 561 half-space soil model.

562

563 To further demonstrate the more severe near-field effects associated with amplitude decay,
 564 Figure 5d presents the simulated wavefield ellipticity, expressed through the horizontal-to-
 565 vertical (H/V) ratio of particle displacement amplitude, measured with distance in wavelengths
 566 for the same frequencies outlined in Figure 5b. The ellipticity also displays oscillations that

567 decrease and stabilize at normalized distances greater than about $10 \lambda_R$ from the source. This
568 observation underscores that the near-field amplitude decay oscillations stem from body
569 waves, as Rayleigh wave ellipticity in a half-space is determined solely by Poisson's ratio
570 (Tokimatsu 1995) and should not oscillate. In Figure 5d, we observe that the calculated
571 ellipticities oscillate around the theoretical value of approximately 0.64 anticipated for
572 Rayleigh wave ellipticity in a viscoelastic half-space with Poisson's ratio equal to 0.33,
573 depicted by the dotted horizontal line in Figure 5d.

574 The synthetic time histories recorded by the C1000 at 2 km and the C1000 at 5 km MAM
575 arrays (refer to Figures 4 and 5) were processed using the FDBF and NFDBFa methods to
576 estimate phase velocity and attenuation, respectively, as illustrated in Figure 6. Figure 6 aims
577 to highlight the impact of wave amplitude decay patterns on the attenuation estimates. In terms
578 of abilities to resolve phase velocity, both the C1000 arrays seem to perform approximately the
579 same, whether 2 km away from the source (Figure 6a) or 5 km away from the source (Figure
580 6b). However, upon inspecting Figures 6c and 6d, it becomes evident that the array located 5
581 km from the source (i.e., Figure 6d) provides more reliable attenuation estimates at lower
582 frequencies compared to the array closer to the source. This observation can be explained by
583 referring to Figure 5b, where the amplitude decay patterns measured by the array positioned 2
584 km from the source are shaded in pink. It is apparent that in close proximity to the source, the
585 low-frequency waves have not traveled a sufficient number of wavelengths, resulting in
586 amplitude decay that does not conform to pure exponentials (i.e., linear decay in log scale).
587 However, by the time these waves reach the array positioned 5 km from the source (blue
588 shading in Figure 5b), the oscillations in amplitude decay have diminished significantly,
589 approaching a pure exponential decay. Therefore, it is noteworthy that in an ambient-noise
590 survey, even though the source location is unknown, if the noise source is close to the array in
591 terms of wavelengths traveled by the desired frequency, it may lead to unreliable and scattered
592 attenuation results. Nonetheless, Figures 6c and 6d clearly demonstrate the reliability of the
593 new NFDBFa approach in retrieving phase attenuation estimates over a broad range of
594 frequencies.



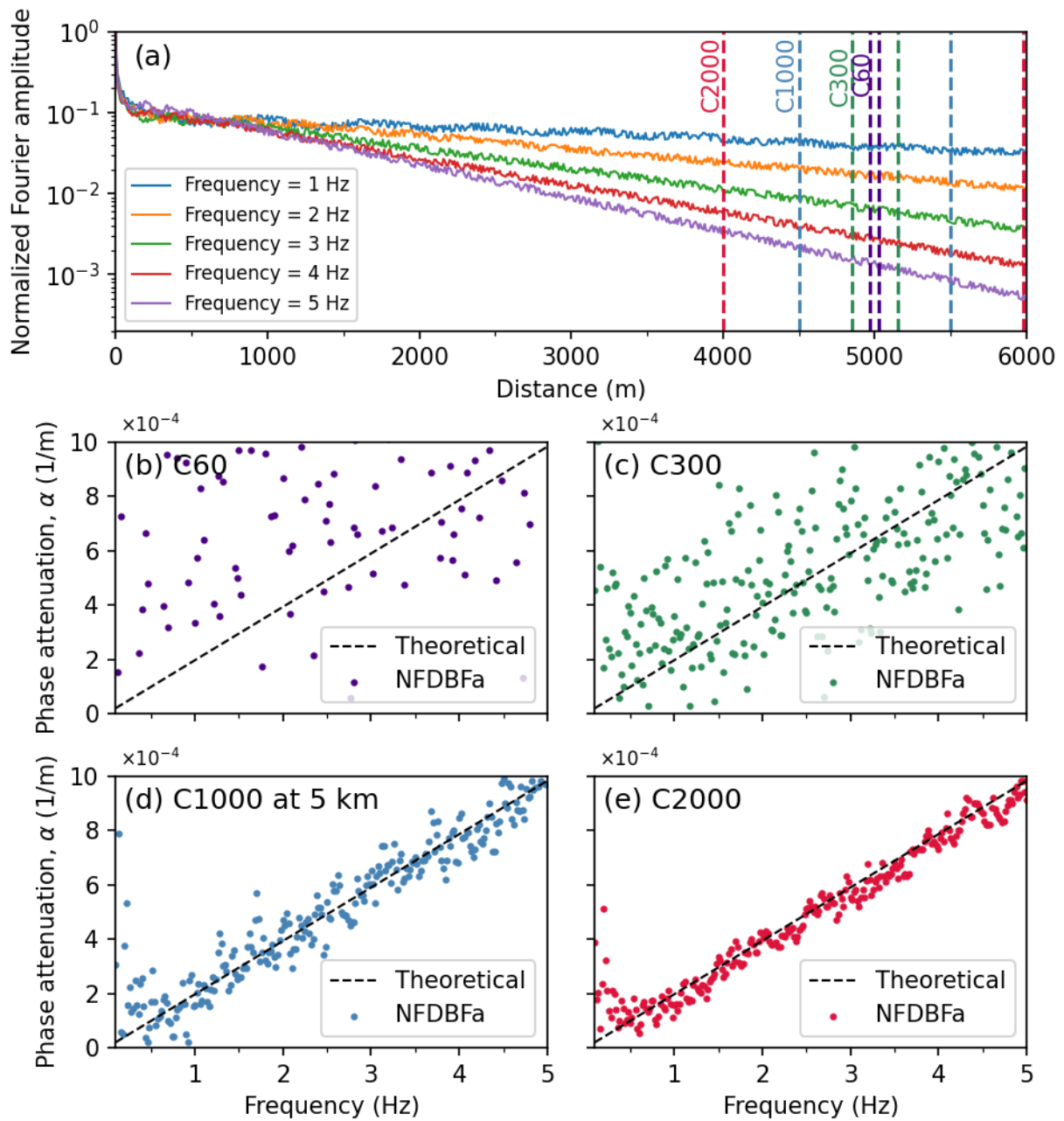
595

596 **Figure 6.** Half-space wavefield simulation: phase velocity (top) and phase attenuation (bottom)
 597 dispersion data estimated with FDBF and NFDBFa, respectively, from 1 km arrays positioned at two
 598 distinct distances from the ambient noise source: (left) at two kilometers (C1000 at 2 km), and (right)
 599 at five kilometers (C1000 at 5 km).

600

601 Finally, the performance of the NFDBFa in the presence of incoherent noise is investigated.
 602 For this purpose, Figure 7 illustrates the influence of incoherent noise and array size on phase
 603 attenuation estimates using the same half-space simulation results. The analysis focuses on the
 604 four arrays of different sizes concentrically-centered 5 km from the source (refer to Figures 4
 605 and 5a). Incoherent noise was introduced to the signal, with a target signal-to-noise ratio (SNR)
 606 at 20 dB, which resulted in the frequency-dependent amplitude decay patterns depicted in
 607 Figure 7a (compared to Figure 5b). Figures 7b, 7c, 7d, and 7e display the attenuation estimates
 608 obtained using the C60, C300, C1000, and C2000 MAM arrays, respectively. It becomes
 609 evident that larger arrays yield more accurate attenuation estimates in the presence of
 610 incoherent noise. Figure 7a elucidates the rationale behind this enhanced performance for
 611 larger arrays across all frequencies. The C2000 MAM array samples a significantly larger area,
 612 enabling it to discern the exponential amplitude decay even in the presence of noise. The C60

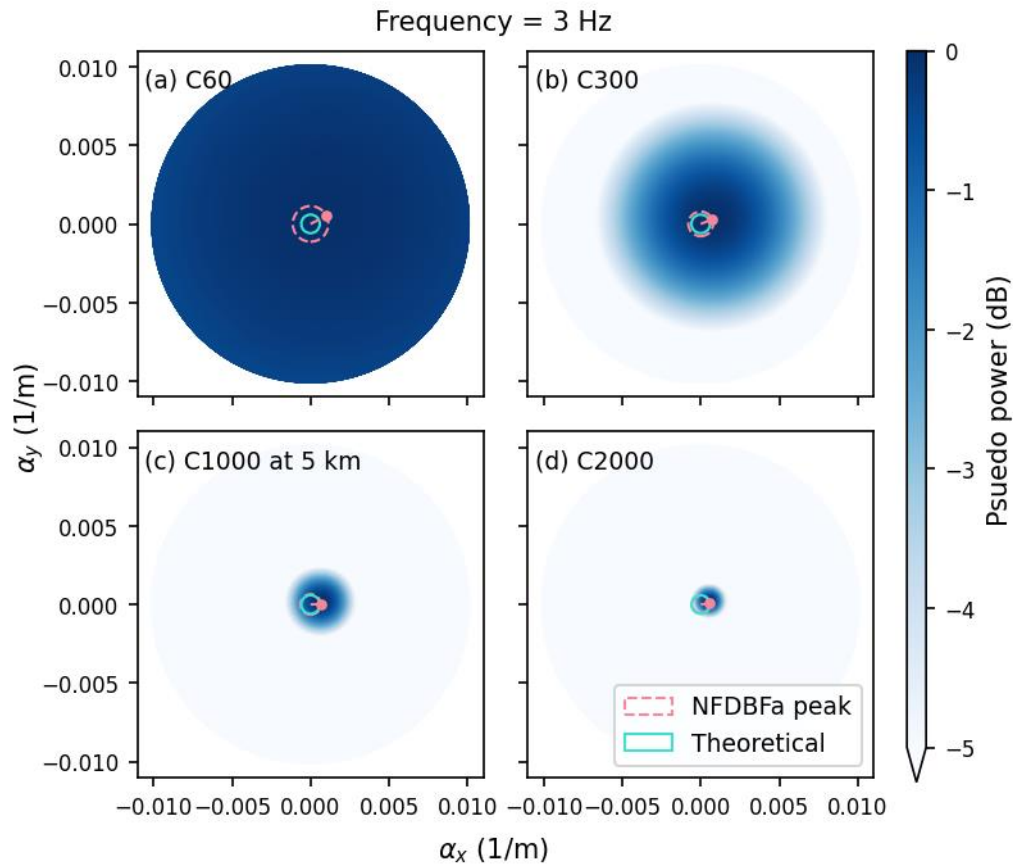
613 MAM array samples a significantly smaller area, and thus is considerably more sensitive to
 614 amplitude fluctuations caused by incoherent noise, resulting in the significant scatter observed
 615 in the attenuation estimates shown in Figure 7b.



616

617 **Figure 7.** Half-space wavefield simulation with noise: Panel (a) shows the amplitude decay of the same five frequencies depicted in Figure 5 but now with added incoherent noise to the signal, setting the
 618 signal-to-noise ratio (SNR) at 20 dB. Panels (b) to (e) present the predicted phase attenuation data from the NFDBFa analysis for four arrays concentrically-centered at five kilometers from the source, with
 619 diameters of 60 m (C60), 300 m (C300), 1 km (C1000 at 5 km), and 2 km (C2000), respectively.
 620
 621
 622

623 Figure 8 further illustrates the impact of array size on resolving attenuation coefficients by
 624 showcasing the $f-\vec{\alpha}$ spectra for a frequency of 3 Hz that were calculated from the wavefield
 625 recorded by the four concentrically-centered arrays located 5 km from the source. Notably, the
 626 mainlobe (dark blue shaded area) is considerably narrower for larger arrays, resulting in more
 627 reliable estimates of phase attenuation. Two key points warrant attention here. First, the
 628 feasibility of employing larger arrays might be restricted due to limitations in access at a given
 629 site, or to help maintain approximately a one-dimensional (1D) subsurface condition beneath
 630 the array, which is an implicit assumption in the analysis technique (i.e., no lateral spatial
 631 variability). Meeting this assumption becomes more challenging as the array size expands.
 632 Second, it is essential to highlight that the method used to determine the optimal MAM array
 633 size for attenuation estimates differs from the one employed in obtaining phase velocity
 634 estimates. In dispersion estimation, smaller MAM arrays are more effective at capturing high
 635 frequency phase velocities, whereas larger arrays are better suited for resolving lower
 636 frequency phase velocities (Foti et al., 2018; Vantassel and Cox, 2022). However, according to
 637 the results depicted in Figure 7, the larger arrays demonstrated superior ability in resolving
 638 phase attenuation across the entire considered frequency range compared to the smaller arrays.



640 **Figure 8.** Half-space wavefield simulation with noise: Panels (a) through (d) present the $f-\vec{\alpha}$ spectra
641 obtained through NFDBFa analysis for a frequency of 3 Hz. The spectra are derived from the wavefield
642 recorded by the four arrays concentrically-centered five kilometers from the source with diameters of
643 60 m (C60), 300 m (C300), 1 km (C1000), and 2 km (C2000), respectively, as depicted in Figure 7.

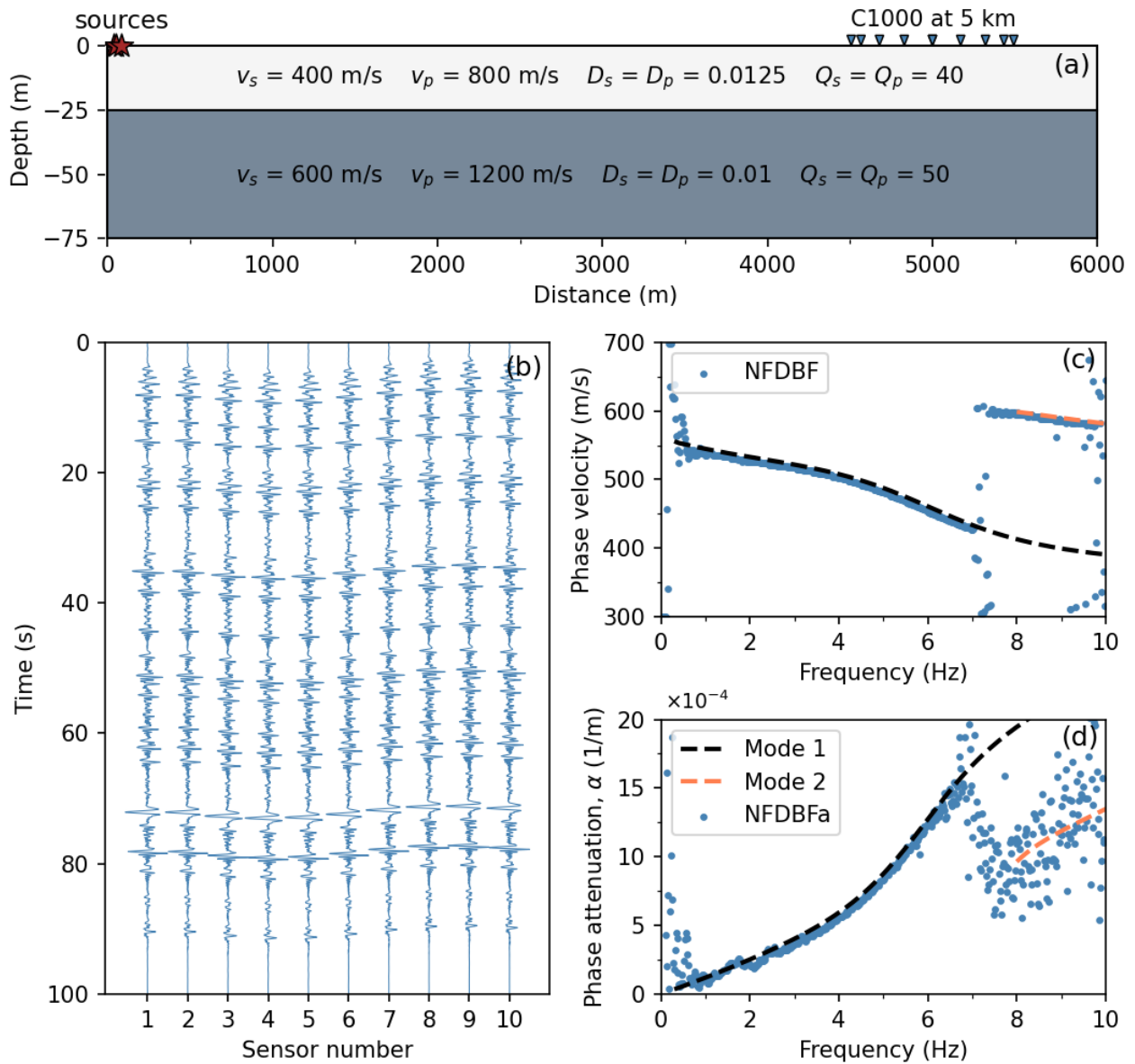
644 **Layer above a half-space model**

645 The performance of the NFDBFa approach on a synthetic model consisting of a single layer
646 above a half-space is illustrated in this subsection. The model's constitutive small-strain
647 parameters and the source and receiver configurations are provided in Figure 9a. For this
648 synthetic study, 150 vertical point sources with varying forcing functions and trigger times
649 were activated. The sources were triggered five kilometers away from the center of a one-
650 kilometer diameter circular array consisting of 10 sensors: one in the center and nine equally
651 distributed around its perimeter (just like the C1000 at 5 km MAM array depicted in Figure 4).
652 The waveforms recorded by the array are depicted in Figure 9b. These waveforms were
653 subsequently processed using FDBF and NFDBFa to derive the Rayleigh wave phase velocity
654 dispersion data shown in Figure 9c and the phase-attenuation data shown in Figure 9d,
655 respectively. The theoretical Rayleigh-wave phase velocity dispersion and attenuation curves
656 for the model are also presented in Figures 9c and 9d, respectively. In these figures, the
657 fundamental theoretical mode is denoted as Mode 1, while the 1st-higher mode is denoted as
658 Mode 2.

659 The FDBF method is able to extract experimental phase velocity dispersion data from the
660 synthetic wavefield that well-matches the theoretical dispersion curves and captures the
661 transition from Mode 1 to Mode 2 at approximately 7 Hz. A strong agreement is also observed
662 between the theoretical attenuation curves and the experimental attenuation data extracted from
663 the synthetic wavefield using the NFDBFa method, particularly for Mode 1. The attenuation
664 data shifts to Mode 2 at the same frequency where the phase velocity dispersion data transitions
665 to Mode 2. A similar observation regarding the relation between the frequencies at which phase
666 velocity and attenuation mode transitions occur was also reported by Aimar et al. (2024a) using
667 MASW data. The observation that phase velocity and phase attenuation data tend to shift modes
668 at identical frequencies is potentially significant, as patterns in attenuation modes are generally
669 more complex than those in phase velocity modes.

670 The effectiveness of the proposed NFDFBa approach has been successfully demonstrated
671 through the analyses conducted on synthetic datasets, as discussed above. Now, we shift our

672 focus to applying this approach to real field data, offering a thorough demonstration of its
 673 effectiveness in a practical, real-world situation.



674
 675 **Figure 9.** Layered model simulation: Panel (a) presents the soil properties utilized in the simulation
 676 for the soil layer and the half-space, along with the surface sources and 1-km receiver array located 5
 677 km from the source (C1000 at 5 km). Panel (b) displays the waveforms collected from the C1000 array.
 678 In Panel (c), the good agreement between the theoretical Rayleigh-wave phase velocity curves (Mode
 679 1 and Mode 2) and the experimental phase velocity data obtained through the FDBF approach on the
 680 original wavefield is demonstrated. Finally, Panel (d) showcases the good agreement between the
 681 theoretical modal attenuation curves and the experimental modal attenuation data extracted from the
 682 converted wavefield using the proposed NFDBFa approach are depicted.

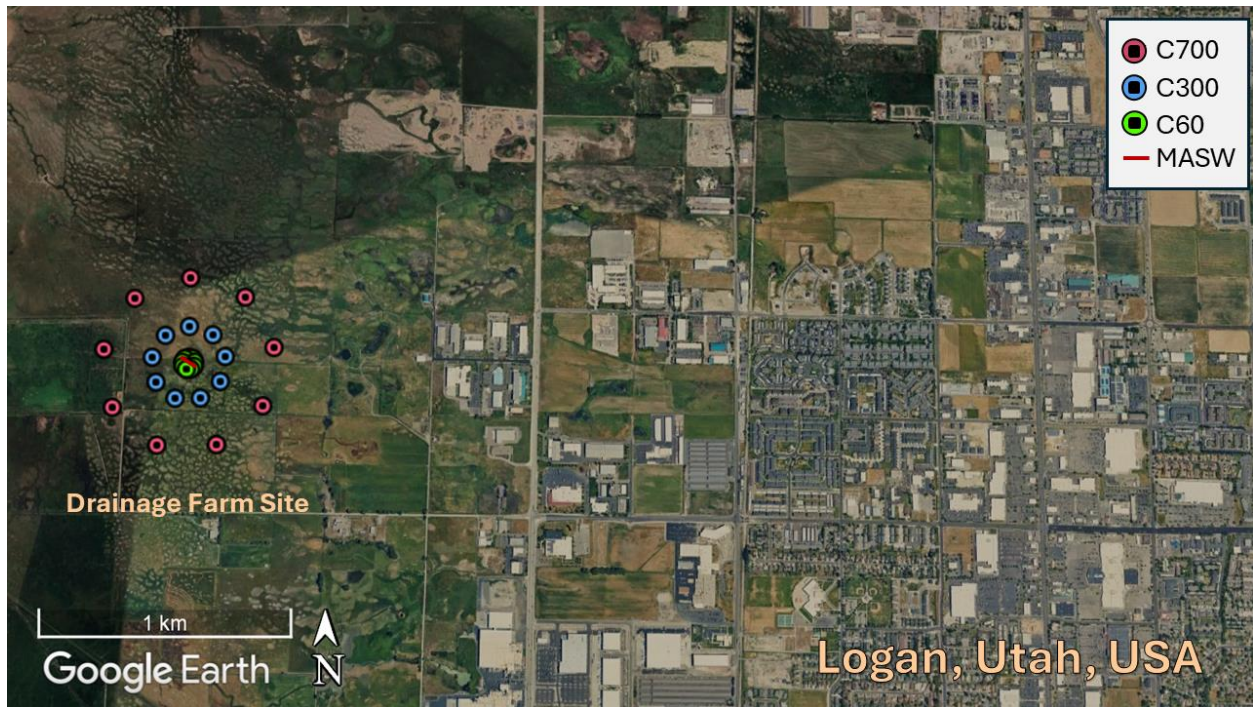
683

684 **FIELD APPLICATION AND VALIDATION**

685 A surface wave field-testing campaign was conducted at the Drainage Farm Site in Logan,
686 Utah, USA (refer to Figure 10), a property owned by Utah State University (USU). Structural
687 geology indicates that Southern Cache Valley, encompassing the Drainage Farm Site and
688 located in the northeastern part of the Basin and Range province, is a graben bounded by high-
689 angle normal faults (Williams, 1962). The site is underlain by Paleozoic rocks, which are
690 overlain by Tertiary formations such as the Wasatch and Salt Lake formations, composed of
691 conglomerate, siltstone, and tuffaceous sandstone. In certain areas of Cache Valley, these
692 formations reach thicknesses of up to 2,440 m (Evans et al., 1996). The near-surface geology
693 of the Drainage Farm Site is characterized by sediments from ancient Lake Bonneville, which
694 receded to form the Provo shoreline. These sediments include alluvial, lacustrine, and deltaic
695 deposits (Williams, 1962; Evans et al., 1996). Well logs presented by Williams (1962) reveal
696 alternating layers of silt and clay, sand, and gravel above the Salt Lake formation. Moreover,
697 limited deep well logs from the vicinity of the Drainage Farm Site indicate that rock can be
698 encountered at depths ranging from 176 m to more than 350 m (Perez, 1969).

699 The goal of the testing was to collect a high-quality surface wave dataset that could be used for
700 attenuation studies to validate the proposed NFDBFa technique. The field testing involved both
701 active-source MASW testing and ambient noise MAM testing. The sensor array configurations
702 utilized for MASW and MAM at the Drainage Farm Site are illustrated in Figure 10. MASW
703 testing was performed using 24, 4.5-Hz vertical geophones placed with a spacing of two meters
704 between successive geophones, resulting in an array length of 46 m. Wavefields with strong
705 Rayleigh wave content were actively generated by striking vertically on a strike-plate with a
706 sledgehammer. The sledgehammer was used at eight distinct "shot" locations that were offset
707 by 5, 10, 15, and 20 m relative to the first/last geophone off each end of the array. Five distinct
708 sledgehammer blows were recorded at each location for subsequent stacking to increase the
709 signal-to-noise ratio (Foti et al. 2018). MAM testing utilized three concentric circular arrays
710 that were aligned with the middle of the MASW array, as depicted in Figure 10. The three
711 arrays were 700-m, 300-m, and 60-m in diameter, and will be referred to as C700, C300, and
712 C60, respectively. Each array consisted of nine evenly distributed three-component broadband
713 seismometers (Nanometrics Inc. Trillium Compact 120s seismometers) along its circumference
714 to capture ambient vibrations. The three arrays did not record data simultaneously; instead, the
715 nine sensors were used to collect noise data for each of the MAM arrays one array at a time.
716 First, the sensors recorded seismic noise for 13 hours and 30 minutes for the C700 array.

717 Subsequently, the sensors were relocated to their designated locations for the C60 and C300
718 arrays, recording ambient noise for an hour and a half and three hours, respectively.



719

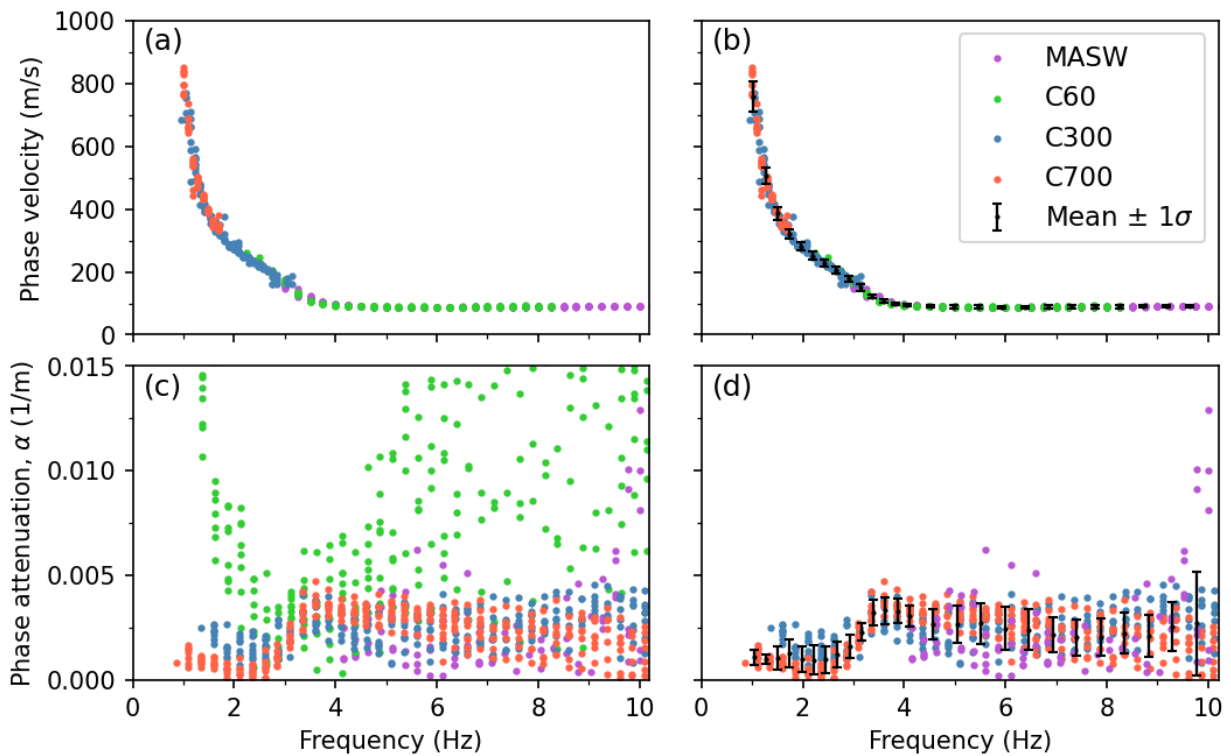
720 **Figure 10.** Plan view of the MASW and MAM arrays employed for testing at the Drainage Farm Site
721 in Logan, Utah, USA. The concentric MAM arrays featured diameters of 60 m (C60), 300 m (C300),
722 and 700 m (C700), while the MASW array comprised 24, 4.5-Hz vertical geophones, spanning 46 m.

723

724 For Rayleigh-wave phase velocity dispersion analysis, MASW data were analyzed using the
725 FDBF method with cylindrical-wave steering (Zywicki and Rix, 2005), as coded in the open-
726 source surface wave processing package swprocess (Vantassel, 2021). This processing was
727 coupled with the multiple source-offset technique for identifying near-field contamination and
728 quantifying dispersion uncertainty (Cox and Wood, 2011; Vantassel and Cox, 2022). As a
729 result, eight phase velocity estimates were obtained for each frequency, corresponding to one
730 phase velocity estimate from each of the eight shot locations. MASW Rayleigh wave dispersion
731 data influenced by near-field effects or significant offline noise were trimmed before
732 calculating phase velocity dispersion statistics.

733 The three-component beamforming approach (Wathelet et al., 2018) coded in the open-source
734 software package Geopsy (Wathelet et al., 2020) was used to generate Rayleigh-wave phase
735 velocity dispersion data for each of the MAM arrays. The recorded time for each array was
736 discretized into blocks, with each block further divided into at least 30-time windows. The

737 window lengths were selected to contain at least 30 cycles (periods) at the lowest processing
 738 frequency that could be extracted from each MAM array (Vantassel and Cox, 2022). For each
 739 MAM array, eight phase velocity estimates were extracted at each analyzed frequency using
 740 the three-component beamforming (Wathelet et al., 2018) approach to ensure consistency with
 741 the eight phase velocity estimates obtained from the MASW processing. Spurious dispersion
 742 data stemming from high-amplitude noise in the near-field (e.g., traffic noise close to the
 743 sensors) and incoherent noise were manually eliminated before calculating dispersion statistics.
 744 Ambient noise phase velocity dispersion data from all MAM arrays were combined with the
 745 active phase velocity dispersion data obtained from MASW processing, as shown in Figure
 746 11a. The combined data, used to compute mean and \pm one standard deviation dispersion
 747 estimates (Vantassel and Cox, 2022), are displayed in Figure 11b relative to the individual
 748 MASW and MAM dispersion data points for the Drainage Farm Site.



749

750 **Figure 11.** Experimental phase velocity and attenuation data extracted from MASW and MAM testing
 751 at the Drainage Farm Site in Logan, UT, USA. Panel (a) displays the experimental phase velocity
 752 dispersion data of Rayleigh waves processed from an MASW array and three circular MAM arrays,
 753 with diameters of 60 m, 300 m, and 700 m. Panel (b) showcases the mean and \pm one standard deviation
 754 of the experimental Rayleigh wave phase velocity dispersion data derived from the combined MASW
 755 and MAM datasets. Panel (c) displays the experimental phase attenuation data from MASW and three
 756 circular MAM arrays. Panel (d) illustrates the mean \pm one standard deviation of the experimental phase
 757 attenuation data calculated from the combined MASW, C300, and C700 MAM arrays.

758

759 The cylindrical FDBFa (CFDBFa) approach, as proposed by Aimar et al. (2024a), was
760 employed to derive attenuation estimates from the MASW data. The CFDBFa algorithm
761 accounts for Rayleigh wave geometric spreading by considering the cylindrical shape of the
762 wavefront. Mirroring the MASW phase velocity dispersion analysis, the multiple source-offset
763 technique was utilized for quantifying attenuation uncertainty. Thus, eight attenuation
764 estimates were extracted from the MASW data at each analyzed frequency using CFDBFa. For
765 the MAM attenuation estimates, the new NFDBFa approach introduced in this study was
766 employed. Geometric spreading was not accounted for, as the distance between the MAM
767 arrays and the ambient noise sources was unknown. However, no nearby sources were observed
768 during acquisition, so we believe that the plane wave approximation is acceptable. The
769 recorded time for each array was discretized into eight blocks, with each block further divided
770 into 30 windows. Consequently, the window length employed for each MAM array can be
771 determined by dividing the total recording time of the array by the product of 8 blocks and 30
772 windows (i.e., 240). Similar to MAM phase velocity dispersion analysis, the window lengths
773 were selected to contain at least 30 periods at the lowest processing frequency that could be
774 extracted from each MAM array (Vantassel and Cox, 2022). Averaging the estimates from all
775 windows within each block yielded a single data point per block, thus providing eight unique
776 attenuation estimates per frequency. This processing approach ensured that an equal number of
777 attenuation data points were obtained at each frequency for all of the MASW and MAM arrays.
778 The combined ambient-noise attenuation data from all MAM arrays and the active attenuation
779 data from the MASW array are plotted together in Figure 11c. A good agreement is observed
780 between the attenuation estimates derived from the MASW array and those obtained from the
781 C300 and C700 arrays for frequencies ranging from 4 to 10 Hz. The MASW testing did not
782 generate coherent attenuation data at frequencies less than 4 Hz, due to the limitations of the
783 active sledgehammer source. However, the MAM testing was able to extract coherent
784 attenuation data at frequencies below 1 Hz. The agreement observed between the active-source
785 and ambient noise attenuation estimates serves as compelling evidence for the efficacy of the
786 proposed NFDBFa approach. However, it is notable that there is significant scatter in the
787 attenuation estimates obtained using the C60 array. This variability is likely caused by the
788 challenges previously discussed in regards to using smaller MAM arrays for attenuation
789 studies, as the phase velocity data extracted from the C60 array was very good (refer to Figure

790 11a). Hence, the attenuation data from the C60 array was removed prior to calculating
791 attenuation statistics. The combined attenuation estimates from the MASW, C300, and C700
792 arrays, and the mean and \pm one standard deviation attenuation estimates obtained from those
793 three arrays, are depicted in Figure 11d. While a noticeable agreement exists among the three
794 arrays, there is significantly greater scatter in the attenuation estimates (Figure 11d) compared
795 to the phase velocity dispersion estimates (Figure 11c). Quantitatively, the coefficient of
796 variation (i.e., the standard deviation normalized by the mean) for the phase velocity
797 experimental data ranges between 0.05 and 0.07, whereas the coefficient of variation for phase
798 attenuation is generally an order of magnitude larger, around 0.5 and increasing up to 0.6-0.8
799 at high frequencies. The larger uncertainty observed at frequencies above 9.5 Hz in Figure 11d
800 results from the divergence between the MASW and MAM attenuation estimates, which may
801 stem from the inability of the MAM arrays in this experiment to provide reliable attenuation
802 estimates beyond this frequency. Nonetheless, the coefficient of variation values of the
803 experimental attenuation data are consistent with results reported by several other studies (e.g.,
804 Rix et al., 2000; Garofalo et al., 2016; Aimar, 2022). The application of the new NFDBFa
805 approach in this field test showcases its effectiveness in estimating attenuation coefficients
806 from ambient noise wavefield data.

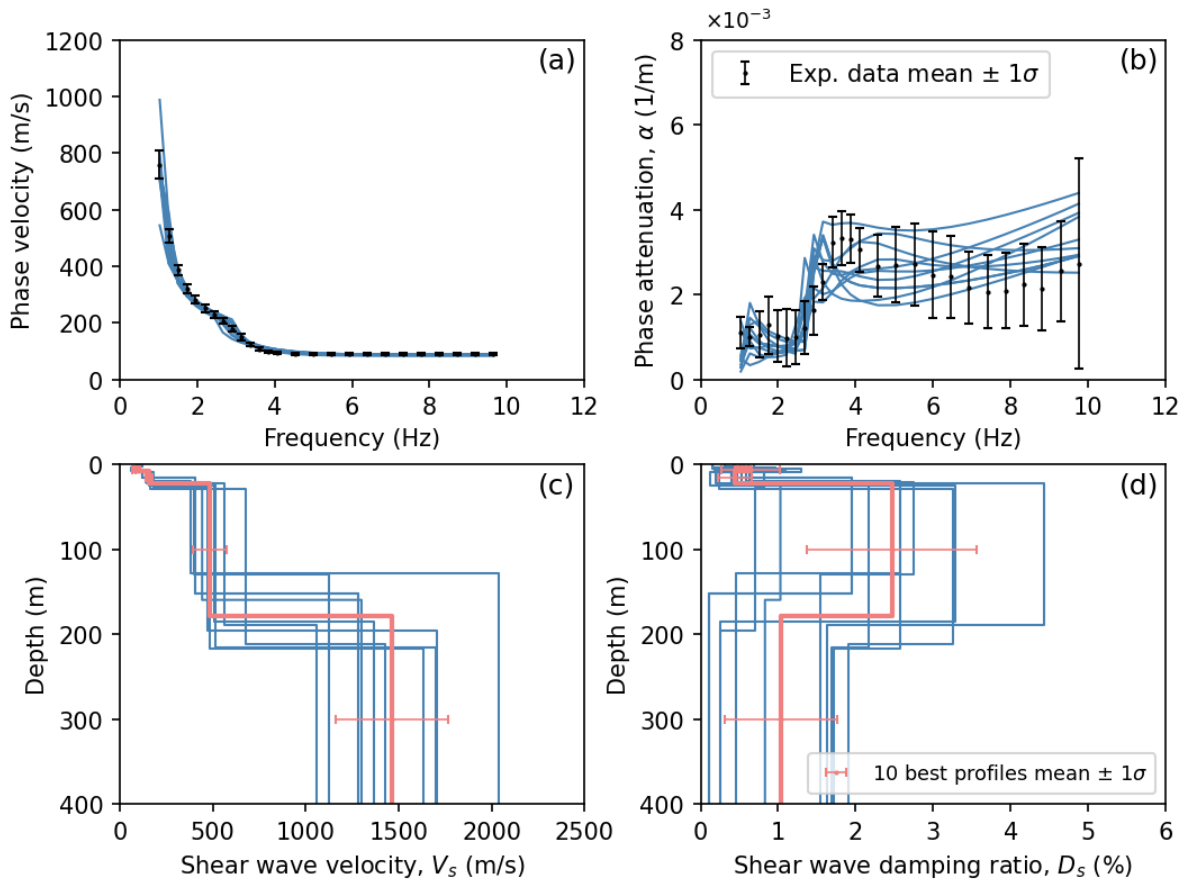
807 Finally, the statistical experimental Rayleigh-wave phase velocity and attenuation parameters
808 derived from both the MASW and MAM testing (refer to Figures 11b and 11d) were used to
809 invert for V_s and D_s profiles at the Drainage Farm Site. This was achieved through the Monte
810 Carlo-based joint inversion of phase velocity and phase attenuation data developed by Aimar
811 et al. (2024b). Although the effectiveness of the joint inversion procedure has been proven for
812 active surface wave data (Lai and Rix, 1998; Aimar et al., 2024b), its application to combined
813 dispersion data from MASW and MAM testing, covering a broad frequency range, is novel.
814 This is because past studies on inverting MAM-based attenuation data to retrieve damping
815 properties at large depths typically adopted an uncoupled inversion approach, based on a
816 separate inversion of Rayleigh-wave phase velocity and α (e.g., Prieto et al., 2009; Parolai,
817 2014).

818 The inversions performed herein involved 50,000 five-layer trial soil models with
819 progressively increasing thicknesses, covering a comprehensive range of layer thicknesses, V_s ,
820 and D_s values. The layering was informed by a preliminary inversion study based solely on
821 phase velocity dispersion data, which is omitted here for simplicity. Realistic values were fixed

822 for the Poisson's ratio and mass densities. The D_p/D_s ratio was treated as an adjustable
823 parameter, guided by various trials and informed by engineering judgment. Ultimately, we
824 adopted a constant D_p/D_s ratio of 1.4, similar to the approach taken by Bergamo et al. (2023).
825 Forward dispersion and attenuation modeling were conducted using the Computer Programs
826 for Seismology software (Herrmann, 2013). The fit to the experimental data was quantitatively
827 assessed using a normalized root mean square (RMS) error that accounts for estimation
828 uncertainty, similar to the metric proposed by Wathelet et al. (2004).

829 The ten best inversion results, which are those that achieved the lowest RMS error between
830 their theoretical phase velocity and phase attenuation curves and the experimental data
831 statistics, are shown in Figure 12. The theoretical phase velocity and attenuation curves are
832 shown relative to the experimental data error bars in Figures 12a and 12b, respectively. The
833 ten best V_s and D_s profiles, along with their mean and \pm one standard deviation, are shown in
834 Figures 12c and 12d, respectively, extending down to a depth of 400 m, which is approximately
835 half of the maximum resolved phase velocity wavelength. The V_s profiles in Figure 12c
836 collectively feature a shallow layer about 25 m thick with velocities ranging from
837 approximately 90 to 185 m/s, including a low-velocity zone, which is consistent with known
838 near-surface layering. Below this, there is generally a thicker layer extending down to
839 approximately 180 m with velocities varying around 500 m/s. At depths of 150-200 m, a stiff
840 layer with velocities around 1500 m/s is commonly identified across the profiles. These depths,
841 while variable, are consistent with the location of Salt Lake Formation rock surface, as
842 discussed above. The D_s profiles in Figure 12d indicate that damping in the top 25 m is less
843 than 1%. Below this depth, there is a noticeable variability in the estimated D_s values between
844 the ten best profiles, with a coefficient of variation ranging between 0.43 and 0.7. Nonetheless,
845 D_s can be observed to increase to approximately 2% to 4% in the deeper soil deposits, which
846 consist of alternating clay, sand, and gravel layers. At the top of the Salt Lake Formation rock
847 surface, D_s collectively decreases again to less than 2% for all of the ten best profiles. The large
848 variability in D_s is likely due to the complex geology of the site, the significant standard
849 deviation in the experimental attenuation data, and the moderately low sensitivity of theoretical
850 attenuation curves to D_s at greater depths (e.g., Badsar et al., 2012; Aimar et al., 2024b).
851 Despite these challenges, the joint inversion procedure provided in-situ estimates of D_s at
852 depths not reached by conventional site characterization techniques. This confirms the
853 advantages of combining MASW and MAM data for the combined estimation of stiffness and

854 dissipation parameters of soil deposits. While the results are promising, additional validation
 855 through laboratory or invasive testing will help confirm the accuracy of the D_s estimates.
 856 Continued efforts to improve attenuation estimation techniques and refine the joint phase
 857 velocity and attenuation inversion algorithm will further enhance the reliability of subsurface
 858 D_s estimation through noninvasive testing.
 859



860

861 **Figure 12.** Inversion results for the experimental Rayleigh-wave phase velocity and attenuation data
 862 collected at the Drainage Farm Site in Logan, UT, USA. The figure highlights the ten best-fitting
 863 models, with Panels (a) and (b) comparing the theoretical curves for phase velocity and attenuation,
 864 respectively, against the experimental data represented by mean values with \pm one standard deviation
 865 error bars. Panels (c) and (d) display the ten best V_s and D_s profiles along with their mean and \pm one
 866 standard deviation, respectively.

867

868 CONCLUSIONS

869 A new methodology for estimating frequency-dependent attenuation coefficients through the
 870 analysis of ambient noise wavefield data recorded by 2D arrays of surface seismic sensors has
 871 been presented. The approach relies on the application of an attenuation-specific wavefield

872 conversion and frequency-domain beamforming (FDBF). It has been termed the noise FDBF
873 attenuation (NFDBFa) method. Importantly, using an FDBF approach, as opposed to a noise
874 cross-correlation approach, enables the direction of ambient noise propagation to be
875 determined for each noise window and frequency, and does not require an equipartitioned
876 ambient noise wavefield. Furthermore, using an FDBF approach enables the phase velocity
877 and attenuation data generated from active-source testing like MASW to be combined with
878 phase velocity and attenuation data generated from ambient noise testing like MAM in order
879 to span a broader frequency range. This enables the joint inversion of phase velocity and
880 attenuation to be performed as a means to extract shear wave velocity and small-strain damping
881 ratio profiles to significantly greater depths than previously possible using only active-source
882 data.

883 2D plane strain numerical simulations were conducted to deepen our understanding of the
884 proposed NFDBFa method. These simulations aimed to evaluate how the proximity of the
885 MAM array to the noise source, the presence of incoherent noise, and the size of the array
886 affect the estimates of phase attenuation. The results demonstrated that near-field effects are
887 more pronounced and extend over greater distances for phase attenuation estimates in
888 comparison to those considered for phase velocity estimation. Furthermore, it was discovered
889 that larger array sizes consistently provided more accurate phase attenuation estimates across
890 all considered frequencies, contrary to the conventional MAM design criteria used for phase
891 velocity dispersion estimation, where larger arrays are typically preferred for resolving lower
892 frequencies while smaller arrays excel at resolving higher frequencies. This distinction
893 emphasizes the need for unique design criteria when planning a MAM array for attenuation
894 estimation.

895 The proposed NFDBFa approach underwent validation through numerical wave propagation
896 simulations, comparing predicted frequency-dependent phase attenuation values against
897 theoretical phase attenuation curves for two synthetic models. Furthermore, validation of the
898 developed technique was reinforced using MASW and MAM field data collected at the
899 Drainage Farm Site in Logan, Utah, USA. The phase velocity and attenuation data extracted
900 from the MASW and MAM recordings agreed well over a common bandwidth, while the
901 ambient noise MAM data allowed the phase velocity and attenuation estimates to be extracted
902 at significantly lower frequencies. The joint inversion of the experimental Rayleigh-wave
903 phase velocity and phase attenuation data obtained from both MASW and MAM testing

904 facilitated the estimation of shear wave velocity and small-strain damping ratio profiles to
905 significant depths (400 m) at the Drainage Farm Site. While these results are promising, they
906 still need to be validated through additional invasive and/or laboratory testing.

907 As noted herein and in other studies like Aimar et al. (2024a), attenuation data are significantly
908 more variable and more complex to understand (e.g., modal curves that repeatedly cross one
909 another) than phase velocity data. As such, there is a need for future studies to better understand
910 attenuation data and how to invert them to retrieve reliable in-situ profiles of the small-strain
911 damping ratio. Future efforts should involve additional numerical and experimental testing of
912 diverse subsurface conditions, coupled with comparisons to damping estimates obtained from
913 invasive tests such as cross-hole and downhole testing. With the validity of this approach
914 demonstrated on the vertical component, future research will also explore the utilization of the
915 three components of the noise wavefield to enhance attenuation estimates beyond the current
916 method's capabilities.

917 **DECLARATION OF COMPETING INTEREST**

918 The authors declare that they have no known competing financial interests or personal
919 relationships that could have appeared to influence the work reported in this paper.

920 **ACKNOWLEDGEMENTS**

921 The numerical simulations were run on the Texas Advanced Computing Center's (TACC's)
922 cluster Lonestar6, with an allocation provided by DesignSafe-CI (Rathje et al., 2017). This
923 work was supported by the U.S. National Science Foundation (NSF) Grant Number CMMI-
924 2120155. However, any opinions, findings, conclusions, or recommendations expressed in this
925 article are those of the authors and do not necessarily reflect the views of the NSF.

926 **RESEARCH DATA AND CODE AVAILABILITY**

927 The field test data used to validate the NFDBFa approach presented in this paper are available
928 in the dataset by Abbas et al. (2024).

929 **REFERENCES**

- 930 Abbas A, Cox BR, Dawadi N, Jackson N, and Cannon K (2024) Geotechnical site characterization at
931 the Drainage Farm Site. DesignSafe-CI. https://doi.org/10.17603/ds2-sx2h-8s20_v1
- 932 Afanasiev M, Boehm C, van Driel M, Krischer L, Rietmann M, May DA, Knepley MG and Fichtner A
933 (2019) Modular and flexible spectral-element waveform modelling in two and three dimensions.
934 Geophysical Journal International, 216(3), 1675–1692. <https://doi.org/10.1093/gji/ggy469>.
- 935 Aimar A (2022) Uncertainties in the estimation of the shear-wave velocity and the small-strain damping
936 ratio from surface wave analysis. Politecnico di Torino.
- 937 Aimar M, Foti S and Cox BR (2024a) Novel Techniques for In-situ Estimation of Shear-wave Velocity
938 and Damping Ratio through MASW testing Part I: A Beamforming Procedure for Extracting
939 Rayleigh-wave Phase Velocity and Phase Attenuation. Geophysical Journal International.
940 <https://doi.org/10.1093/gji/ggae051>.
- 941 Aimar M, Foti S and Cox BR (2024b) Novel Techniques for In-situ Estimation of Shear-wave Velocity
942 and Damping Ratio through MASW testing Part II: A Monte Carlo Algorithm for the Joint
943 Inversion of Phase Velocity and Attenuation. Geophysical Journal International, 237(1), 525-539.
944 <https://doi.org/10.1093/gji/ggae050>
- 945 Albarello D and Baliva F (2009) In-Situ Estimates of Material Damping from Environmental Noise
946 Measurements. In Increasing Seismic Safety by Combining Engineering Technologies and
947 Seismological Data (pp. 73–84). https://doi.org/10.1007/978-1-4020-9196-4_6
- 948 Aki K (1957). Space and Time Spectra of Stationary Stochastic Waves, with Special Reference to
949 Microtremors. Bulletin of the Earthquake Research Institute, 35, 415–459.
- 950 Aki K and Richards PG (1980) Quantitative Seismology, Theory and Methods. Volume I: 557 pp., 169
951 illustrations. Volume II: 373 pp., 116 illustrations. San Francisco: Freeman. Price: Volume I, U.S.
952 \$35.00; Volume II, U.S. \$35.00. ISBN 0 7167 1058 7 (Vol. I), 0 7167 1059 5 (Vol. II). Geological
953 Magazine, 118(2), 208–208. <https://doi.org/10.1017/S0016756800034439>.
- 954 Anderson JG, Lee Y, Zeng Y and Day S (1996) Control of strong motion by the upper 30 meters.
955 Bulletin of the Seismological Society of America, 86(6), 1749–1759.
956 <https://doi.org/10.1785/BSSA0860061749>.
- 957 Anderson J and Hough S (1984). A model for the shape of the Fourier amplitude spectrum of
958 acceleration at high frequencies. *Bulletin of the Seismological Society of America*, 74(5), 1969-
959 1993. <https://doi.org/10.1785/BSSA0740051969>
- 960 Badsar SA, Schevenels M, Haegeman W and Degrande G (2010) Determination of the material
961 damping ratio in the soil from SASW tests using the half-power bandwidth method. Geophysical
962 Journal International, 182(3), 1493–1508. <https://doi.org/10.1111/j.1365-246X.2010.04690.x>.
- 963 Badsar S (2012) In situ determination of material damping in the soil at small deformation ratios.
964 Katholieke Universiteit Leuven.
- 965 Bergamo P, Marano S and Fah D (2023) Joint estimation of S-wave velocity and damping ratio of the
966 near-surface from active Rayleigh wave surveys processed with a wavefield decomposition
967 approach. Geophysical Journal International 233 (3), 1560–1579.
968 <https://doi.org/10.1093/gji/ggad010>.

- 969 Biot MA (1956) Theory of Propagation of Elastic Waves in a Fluid-Saturated Porous Solid. I. Low-
 970 Frequency Range. *The Journal of the Acoustical Society of America*, 28(2), 168–178.
 971 <https://doi.org/10.1121/1.1908239>.
- 972 Capon J (1969) High-resolution frequency-wavenumber spectrum analysis. *Proceedings of the IEEE*,
 973 57(8), 1408–1418. <https://doi.org/10.1109/PROC.1969.7278>.
- 974 Comina C, Foti S, Boiero D and Socco LV (2011) Reliability of V_s , 30 evaluation from surface-wave
 975 tests. *Journal of Geotechnical and Geoenvironmental engineering*, 137(6), 579–586.
 976 [https://doi.org/10.1061/\(ASCE\)GT.1943-5606.0000452](https://doi.org/10.1061/(ASCE)GT.1943-5606.0000452)
- 977 Cox BR and Beekman AN (2011) Intra-Method Variability in ReMi Dispersion and V_s Estimates at
 978 Shallow Bedrock Sites. *Journal of Geotechnical and Geoenvironmental Engineering*, 137(4), pp.
 979 354–362. [https://doi.org/10.1061/\(ASCE\)GT.1943-5606.0000436](https://doi.org/10.1061/(ASCE)GT.1943-5606.0000436)
- 980 Cox BR and Wood CM (2011) Surface Wave Benchmarking Exercise: Methodologies, Results, and
 981 Uncertainties. *GeoRisk* 2011, 845–852. [https://doi.org/10.1061/41183\(418\)89](https://doi.org/10.1061/41183(418)89).
- 982 Crow H, Hunter JA and Motazedian D (2011) Monofrequency in situ damping measurements in Ottawa
 983 area soft soils. *Soil Dynamics and Earthquake Engineering*, 31(12), 1669–1677.
 984 <https://doi.org/10.1016/j.soildyn.2011.07.002>.
- 985 Cupillard P and Capdeville Y (2010) On the amplitude of surface waves obtained by noise correlation
 986 and the capability to recover the attenuation: a numerical approach. *Geophysical Journal*
 987 *International*. <https://doi.org/10.1111/j.1365-246X.2010.04586.x>.
- 988 Evans JP, McCalpin JP and Holmes DC (1996) Geologic Map of the Logan 7.5' Quadrangle, Cache
 989 County, Utah. Miscellaneous Publication 96-1, Utah Geological Survey, a division of Utah
 990 Department of Natural Resources, Salt Lake City, Utah. ISBN 1-55791-375-7.
- 991 Ewing WM, Jardetzky WS, Press F and Beiser A (1957) Elastic Waves in Layered Media. *Physics*
 992 *Today*, 10(12), 27–28. <https://doi.org/10.1063/1.3060203>.
- 993 Foti S (2004) Using transfer function for estimating dissipative properties of soils from surface-wave
 994 data. *Near Surface Geophysics*, 2(4), 231–240. <https://doi.org/10.3997/1873-0604.2004020>.
- 995 Foti S, Lai C, Rix GJ and Strobbia C (2014) *Surface Wave Methods for Near-Surface Site*
 996 *Characterization*. CRC Press. <https://doi.org/10.1201/b17268>.
- 997 Foti S, Hollender F, Garofalo F, Albarello D, Asten M, Bard PY, Comina C, Cornou C, Cox B, Di Giulio
 998 G, Forbriger T, Hayashi K, Lunedei E, Martin A, Mercerat D, Ohrnberger M, Poggi V, Renalier F,
 999 Sicilia D and Socco V (2018) Guidelines for the good practice of surface wave analysis: a product
 1000 of the InterPACIFIC project. *Bulletin of Earthquake Engineering*, 16(6), 2367–2420.
 1001 <https://doi.org/10.1007/s10518-017-0206-7>.
- 1002 Foti S, Aimar M and Ciancimino A (2021) Uncertainties in Small-Strain Damping Ratio Evaluation and
 1003 Their Influence on Seismic Ground Response Analyses (pp. 175–213).
 1004 https://doi.org/10.1007/978-981-16-1468-2_9.
- 1005 Haendel A, Ohrnberger M and Krüger F (2016) Extracting near-surface Q L between 1–4 Hz from
 1006 higher-order noise correlations in the Euroseistest area, Greece. *Geophysical Journal*
 1007 *International*, 207(2), 655–666. <https://doi.org/10.1093/gji/ggw295>.

- 1008 Hall L and Bodare A (2000) Analyses of the cross-hole method for determining shear wave velocities
1009 and damping ratios. *Soil Dynamics and Earthquake Engineering*, 20(1–4), 167–175.
1010 [https://doi.org/10.1016/S0267-7261\(00\)00048-8](https://doi.org/10.1016/S0267-7261(00)00048-8).
- 1011 Herrmann RB (2013) Computer programs in seismology: an evolving tool for instruction and research,
1012 *Seismol. Res. Lett.*, 84, 1081–1088. 10.1785/0220110096.
- 1013 Holzlöhner U (1980) Vibrations of the elastic half-space due to vertical surface loads. *Earthquake
1014 Engineering & Structural Dynamics*, 8(5), 405–414. <https://doi.org/10.1002/eqe.4290080504>.
- 1015 Johnston DH, Toksöz MN and Timur A (1979) Attenuation of seismic waves in dry and saturated rocks:
1016 II. Mechanisms. *Geophysics*, 44(4), 691–711. <https://doi.org/10.1190/1.1440970>
- 1017 Johnson D and Dudgeon D (1993) *Array signal processing: Concepts and techniques*. Englewood Cliffs,
1018 NJ: P T R Prentice Hall.
- 1019 Jongmans D (1990) In-situ attenuation measurements in soils. *Engineering Geology*, 29(2), 99–118.
1020 [https://doi.org/10.1016/0013-7952\(90\)90001-H](https://doi.org/10.1016/0013-7952(90)90001-H).
- 1021 Keilis-Borok V (1989) *Seismic Surface Waves in a Laterally Inhomogeneous Earth* (V. I. Keilis-Borok,
1022 Ed.; Vol. 9). Springer Netherlands. <https://doi.org/10.1007/978-94-009-0883-3>.
- 1023 Ktenidou O, Abrahamson N, Drouet S, and Cotton F (2015). Understanding the physics of kappa (κ):
1024 Insights from a downhole array. *Geophysical Journal International*, 203(1), 678-691.
1025 <https://doi.org/10.1093/gji/ggv315>
- 1026 Lacoss RT, Kelly EJ and Toksöz MN (1969) Estimation of seismic noise structure using arrays.
1027 *Geophysics*, 34(1), 21–38. <https://doi.org/10.1190/1.1439995>
- 1028 Lai CG (1998) Simultaneous inversion of Rayleigh phase velocity and attenuation for near-surface site
1029 characterization. Georgia Institute of Technology.
- 1030 Lai CG, Rix GJ, Foti S and Roma V (2002) Simultaneous measurement and inversion of surface wave
1031 dispersion and attenuation curves. *Soil Dynamics and Earthquake Engineering*, 22(9–12), 923–
1032 930. [https://doi.org/10.1016/S0267-7261\(02\)00116-1](https://doi.org/10.1016/S0267-7261(02)00116-1).
- 1033 Lai CG and Özcebe A (2016) Non-Conventional Lab and Field Methods for Measuring Frequency-
1034 Dependent Low-Strain Parameters of Soil Dynamic Behaviour. *Soil Dynamics and Earthquake
1035 Engineering*, Vol. 91, pp 72–86. <https://doi.org/10.1016/j.soildyn.2016.09.007>
- 1036 Lamb H (1904) On the propagation of tremors over the surface of an elastic solid. *Proceedings of the
1037 Royal Society of London*, 72(477–486), 128–130. <https://doi.org/10.1098/r SPL.1903.0029>.
- 1038 Michaels P (1998) In Situ Determination of Soil Stiffness and Damping. *Journal of Geotechnical and
1039 Geoenvironmental Engineering*, 124(8), 709–719. [https://doi.org/10.1061/\(ASCE\)1090-0241\(1998\)124:8\(709\)](https://doi.org/10.1061/(ASCE)1090-0241(1998)124:8(709)).
- 1041 Nazarian S, Stokoe KH and Hudson WR (1983) Use of spectral analysis of surface waves method for
1042 determination of moduli and thicknesses of pavement systems. *Transportation Research Record*,
1043 38–45. <https://api.semanticscholar.org/CorpusID:58935998>.
- 1044 O’doherly RF and Anstey NA (1971) Reflections on Amplitudes*. *Geophysical Prospecting*, 19(3),
1045 430–458. <https://doi.org/10.1111/j.1365-2478.1971.tb00610.x>.
- 1046 Ohrnberger M, Schissle E, Cornou C, Wathelet M, Savvaidis A, Scherbaum F, . . . Kind F (2004)
1047 Microtremor array measurements for site effect investigations: Comparison of analysis methods

- 1048 for field data crosschecked by simulated wavefields. 13th World Conference on Earthquake
1049 Engineering. Vancouver, B.C., Canada.
- 1050 Papadopoulos M, François S, Degrande G and Lombaert G (2018) The influence of uncertain local
1051 subsoil conditions on the response of buildings to ground vibration. *Journal of Sound and*
1052 *Vibration*, 418, 200–220. <https://doi.org/10.1016/j.jsv.2017.12.021>.
- 1053 Parolai S (2014) Shear wave quality factor Q_s profiling using seismic noise data from microarrays.
1054 *Journal of Seismology*, 18(3), 695–704. <https://doi.org/10.1007/s10950-014-9440-5>.
- 1055 Parolai S, Lai CG, Dreossi I, Ktenidou OJ and Yong A (2022) A review of near-surface Q_s estimation
1056 methods using active and passive sources. *Journal of Seismology*, 26(4), 823–862.
1057 <https://doi.org/10.1007/s10950-021-10066-5>.
- 1058 Park CB, Miller RD and Xia J (1999) Multichannel analysis of surface waves. *Geophysics*, 64(3), 800–
1059 808. <https://doi.org/10.1190/1.1444590>.
- 1060 Perez M (1969) The Capability of the Utah State University Drainage Farm as an Irrigation and
1061 Drainage Demonstration Project. All Graduate Plan B and other Reports, Spring 1920 to Spring
1062 2023. 623. <https://doi.org/10.26076/6e25-d8ed>.
- 1063 Peterson JR (1993) Observations and modeling of seismic background noise. In. Albuquerque, New
1064 Mexico: United States Geological Survey. 10.3133/ofr93322
- 1065 Prieto GA, Lawrence JF and Beroza GC (2009) Anelastic Earth structure from the coherency of the
1066 ambient seismic field. *Journal of Geophysical Research: Solid Earth*, 114(B7).
1067 <https://doi.org/10.1029/2008JB006067>.
- 1068 Ricker N (1940) The form and nature of seismic waves and the structure of seismograms. *Geophysics*,
1069 5(4), 348–366. <https://doi.org/10.1190/1.1441816>.
- 1070 Richart FE, Hall JR and Woods RD (1970) *Vibrations of Soils and Foundations*. Prentice-Hall.
- 1071 Rix GJ, Lai CG and Spang AW (2000) In Situ Measurement of Damping Ratio Using Surface Waves.
1072 *Journal of Geotechnical and Geoenvironmental Engineering*, 126(5), 472–480.
1073 [https://doi.org/10.1061/\(ASCE\)1090-0241\(2000\)126:5\(472\)](https://doi.org/10.1061/(ASCE)1090-0241(2000)126:5(472)).
- 1074 Rix G, Lai C and Foti S (2001) Simultaneous Measurement of Surface Wave Dispersion and
1075 Attenuation Curves. *Geotechnical Testing Journal*, 24(4), 350.
1076 <https://doi.org/10.1520/GTJ11132J>.
- 1077 Sanchez-Sesma FJ and Campillo MI (2006) Retrieval of the Green's Function from Cross Correlation:
1078 The Canonical Elastic Problem. *Bulletin of the Seismological Society of America*, 96(3), 1182–
1079 1191. <https://doi.org/10.1785/0120050181>.
- 1080 Schevenels M, François S and Degrande G (2009) EDT: An ElastoDynamics Toolbox for MATLAB.
1081 *Computers & Geosciences*, 35(8), 1752–1754. <https://doi.org/10.1016/j.cageo.2008.10.012>.
- 1082 Shibuya S, Mitachi T, Fukuda F and Degoshi T (1995) Strain Rate Effects on Shear Modulus and
1083 Damping of Normally Consolidated Clay. *Geotechnical Testing Journal*, 18(3), 365.
1084 <https://doi.org/10.1520/GTJ11005J>.
- 1085 Snieder R, Wapenaar K and Wegler U (2007) Unified Green's function retrieval by cross-correlation;
1086 connection with energy principles. *Physical Review E*, 75(3), 036103.
1087 <https://doi.org/10.1103/PhysRevE.75.036103>.

- 1088 Spencer TW, Edwards CM and Sonnad JR (1977) Seismic wave attenuation in nonresolvable cyclic
1089 stratification. *Geophysics*, 42(5), 939–949. <https://doi.org/10.1190/1.1440773>.
- 1090 Stoll RD (1974) Acoustic Waves in Saturated Sediments. In *Physics of Sound in Marine Sediments* (pp.
1091 19–39). Springer US. https://doi.org/10.1007/978-1-4684-0838-6_2.
- 1092 Stokoe K, Rix G, Nazarian S (1989) In situ seismic testing with surface waves. 12th International
1093 Conference on Soil Mechanics and Foundation Engineering.
- 1094 Tao Y and Rathje E (2019) Insights into Modeling Small-Strain Site Response Derived from Downhole
1095 Array Data. *Journal of Geotechnical and Geoenvironmental Engineering*, 145(7).
1096 [https://doi.org/10.1061/\(ASCE\)GT.1943-5606.0002048](https://doi.org/10.1061/(ASCE)GT.1943-5606.0002048).
- 1097 Teague DP, Cox BR, Bradley B and Wotherspoon L (2018) Development of Deep Shear Wave Velocity
1098 Profiles with Estimates of Uncertainty in the Complex Inter-Bedded Geology of Christchurch,
1099 New Zealand. *Earthquake Spectra*, 34(2), 639-672. (<https://doi.org/10.1193/041117EQS069M>).
- 1100 Teague DP, Cox BR, and Rathje ER (2018) Measured vs. Predicted Site Response at the Garner Valley
1101 Downhole Array Considering Shear Wave Velocity Uncertainty from Borehole and Surface Wave
1102 Methods. *Soil Dynamics and Earthquake Engineering*, 113(10), 339-355.
1103 <https://doi.org/10.1016/j.soildyn.2018.05.031>.
- 1104 Tokimatsu K (1995) Geotechnical site characterization using surface waves. International Conference
1105 on Earthquake Geotechnical Engineering, ISBN 90-5410-581-X, 1333–1368.
- 1106 Tsai VC (2011) Understanding the amplitudes of noise correlation measurements. *Journal of*
1107 *Geophysical Research*, 116(B9), B09311. <https://doi.org/10.1029/2011JB008483>.
- 1108 Vantassel JP and Cox BR (2020) SWinvert: a workflow for performing rigorous 1-D surface wave
1109 inversions. *Geophysical Journal International*, 224(2), 1141–1156.
1110 <https://doi.org/10.1093/gji/ggaa426>.
- 1111 Vantassel JP (2021) jpvantassel/swprocess: v0.1.0b0. Zenodo <https://doi.org/10.5281/zenodo.4584129>.
- 1112 Vantassel JP and Cox BR (2022) SWprocess: A Workflow for Developing Robust Estimates of Surface
1113 Wave Dispersion Uncertainty, *Journal of Seismology*, 26 (1): 731-756
1114 <https://doi.org/10.1007/s10950-021-10035-y>
- 1115 Verachtert R, Lombaert G and Degrande G (2018) Multimodal determination of Rayleigh dispersion
1116 and attenuation curves using the circle fit method. *Geophysical Journal International*, 212(3),
1117 2143–2158. <https://doi.org/10.1093/gji/ggx523>.
- 1118 Walsh JB (1966) Seismic wave attenuation in rock due to friction. *Journal of Geophysical Research*,
1119 71(10), 2591–2599. <https://doi.org/10.1029/JZ071i010p02591>.
- 1120 Walsh JB (1968) Attenuation in partially melted material. *Journal of Geophysical Research*, 73(6),
1121 2209–2216. <https://doi.org/10.1029/JB073i006p02209>.
- 1122 Wathelet M, Jongmans D and Ohrnberger M (2004) Surface-wave inversion using a direct search
1123 algorithm and its application to ambient vibration measurements. *Near surface geophysics*, 2(4),
1124 211-221. <https://doi.org/10.3997/1873-0604.2004018>
- 1125 Wathelet M, Guillier B, Roux P, Cornou C and Ohrnberger M (2018) Rayleigh wave three-component
1126 beamforming: signed ellipticity assessment from high-resolution frequency-wavenumber

- 1127 processing of ambient vibration arrays. *Geophysical Journal International*, 215(1), 507–523.
1128 <https://doi.org/10.1093/gji/ggy286>.
- 1129 Wathelet M, Chatelain JL, Cornou C, Di Giulio G, Guillier B, Ohrnberger M and Savvaidis A (2020)
1130 Geopsy: A User-Friendly Open-Source Tool Set for Ambient Vibration Processing. *Seismological*
1131 *Research Letters*, 91(3), 1878–1889, doi: 10.1785/0220190360.
- 1132 Williams JS (1962) Lake Bonneville: Geology of Southern Cache Valley, Utah. Geological Survey
1133 Professional Paper 257-C. United States Government Printing Office, Washington, D.C.
- 1134 Winkler, K., and Nur, A. (1982) “Seismic Attenuation: Effects of Pore Fluids and Frictional Sliding.”
1135 *Geophysics*, Vol. 47, pp. 1-15. <https://doi.org/10.1190/1.1441276>
- 1136 Xia J, Miller RD, Park CB and Tian G (2002) Determining Q of near-surface materials from Rayleigh
1137 waves. *Journal of Applied Geophysics*, 51(2–4), 121–129. [https://doi.org/10.1016/S0926-](https://doi.org/10.1016/S0926-9851(02)00228-8)
1138 [9851\(02\)00228-8](https://doi.org/10.1016/S0926-9851(02)00228-8).
- 1139 Zywicki DJ and Rix GJ (2005) Mitigation of Near-Field Effects for Seismic Surface Wave Velocity
1140 Estimation with Cylindrical Beamformers. *Journal of Geotechnical and Geoenvironmental*
1141 *Engineering*, 131(8), 970–977. [https://doi.org/10.1061/\(ASCE\)1090-0241\(2005\)131:8\(970\)](https://doi.org/10.1061/(ASCE)1090-0241(2005)131:8(970)).
- 1142 Zywicki D (1999) Advanced signal processing methods applied to engineering analysis of seismic
1143 surface waves. Georgia Institute of Technology.
- 1144